SKB

Assessing nickel and molybdenum transport in the bedrock at SFL using a dynamic K$_d$ approach

Report for the safety evaluation SE-SFL

Paolo Trinchero

Hedieh Ebrahimi

Elisenda Colas

Daniel Fernàndez-Garcia

SVENSK KÄRNBRÄNSLEHANTERING

Assessing nickel and molybdenum transport in the bedrock at SFL using a dynamic K_d approach

Report for the safety evaluation SE-SFL

Paolo Trinchero, Hedieh Ebrahimi, Elisenda Colas,
Daniel Fernàndez-Garcia

Amphos 21

Summary

A dynamic K_d approach (Trinchero et al. 2016) has been used to assess radionuclide transport in the framework of the SE-SFL evaluation project. First, the influence of the infiltration of altered meteoric water on nickel transport and retention has been simulated by using results of existing reactive transport calculations of the evolution of background geochemistry at the Laxemar site (Sweden). These results, along with the selected mechanistic sorption model for nickel, have provided, by means of the numerical tool iFM (interface to MARFA), spatially and temporary variable values of nickel distribution coefficient (K_d), which have then fed the radionuclide transport code MARFA. The results of the calculations have pointed out that the progressive penetration of diluted altered meteoric water increases significantly the retention capacity of the system (and, thus, decreases substantially nickel discharge at the model boundary). Neglecting this geochemical evolution of the system, as typically done in previous radio-nuclide transport calculations carried out in the framework of other safety evaluation studies for the disposal of nuclear waste in Sweden, leads to overconservative results. In the second part of the project, an analogous approach has been used to evaluate retention mechanisms for molybdenum. This second part of the study has been supported by a detailed and comprehensive study of available data of molybdenum sorption onto iron-bearing minerals; namely goethite and pyrite, and by the development of a new mechanistic surface complexation model. The results of the numerical calculations have shown that molybdenum retention, mostly in the form of molybdate, in the bedrock at Laxemar is modest although not negligible (~16 % of reduction in the peak mass discharge). The overall conclusion of this study is that the dynamic K_d approach and the related software (iFM and MARFA) are mature enough for their use in the context of safety assessment studies for nuclear waste repositories.

Sammanfattning

Modellering med hjälp av angreppssättet "dynamiskt K_d"(Trinchero et al. 2016) har använts för att simulera radionuklidtransport inom ramen för säkerhetsutvärderingsprojektet SE-SFL. Först simulerades inverkan av infiltration av förändrat meteoriskt vatten på nickeltransport och retention med hjälp av resultat från redan befintliga reaktiva transportberäkningar som beskriver utvecklingen av geokemin på platsen Laxemar i Sverige. Dessa resultat har tillsammans med den valda mekanistiska sorptions-modellen för nickel, med hjälp av det numeriska verktyget iFM (gränssnitt till MARFA), använts för att beräkna variabla rumsliga och temporära värden av fördelningskoefficienten (K_d) för nickel som sedan har matats in i radionuklidtransportkoden MARFA. Resultaten av beräkningarna har visat att den progressiva nedträngningen av utspätt förändrat meteoriskt vatten ökar signifikant systemets retentionskapacitet (och sålunda minskar utsläppet av nickel väsentligt vid modellgränsen). Att för-summa den geokemiska utveckling av systemet, som vanligtvis gjorts i tidigare radionuklidtransport-beräkningar utförda inom ramen för andra säkerhetsutvärderingar av slutförvar för kärnavfall i Sverige, leder till överkonservativa resultat. I den andra delen av projektet har en analog metod använts för att utvärdera retentionsmekanismer för molybden. Denna andra del av studien har fått stöd av en detaljerad och omfattande studie av tillgängliga data angående sorption av molybden på järninnehållande mineraler, nämligen goethit och pyrit, samt genom utveckling av en ny mekanisk ytkomplexmodell. Resultaten av de numeriska beräkningarna har visat att retention av molybden, mestadels i form av molybdat, i bergmassan vid Laxemar är blygsam men inte försumbar (ungefär en minskning med 16 % av maxvärdet för massflödet). Den övergripande slutsatsen av denna studie är att tillvägagångssättet med användande av dynamiskt K_d samt den relaterade mjukvaran (iFM och MARFA) är tillräckligt mogna för att användas i samband med säkerhetsbedömningar av slutförvar för kärnavfall.

Contents

1 Introduction

1.1 Background and motivation

A typical approach in modelling radionuclide transport is to lump many complex geochemical retention processes into a single parameter (e.g. the distribution coefficient, K_d), which relates the radionuclide mass retained in the solid phase to its aqueous concentration. This approach relies on an important assumption: the K_d value of each radionuclide is constant in time and space. This assumption could be critical when geochemical conditions are changing significantly (e.g. in the transition from temperate to glacial conditions or due to infiltration processes during the temperate period) as it is demonstrated that the distribution coefficient depends on the pH, redox conditions and major chemistry of the system. Mechanistic geochemical models, which circumvent the above-mentioned limitations, have been widely used in reactive transport calculations in recent years. However, these models are at present too expensive computationally to combine with realistic physical retention processes such as matrix diffusion in a probabilistic framework, which is required in the context of safety assessment for radioactive waste repositories.

A novel "dynamic K_d" approach (sometimes denoted "smart K_d" approach) has been recently presented (Trinchero et al. 2016), which circumvents the aforementioned limitations of constant-K_d calculations. The basic premise of this approach is that the "background" geochemistry (excluding radionuclides) is first to be pre-calculated using a reactive transport code in order to generate a dataset of K_d values in space and time that are representative of the actual geochemical conditions throughout the considered spatial and time domain. This information is then fed to MARFA (Painter and Mancillas 2013) in order to calculate radionuclide transport based on these "dynamic" K_d values. This separation of the major chemistry from radionuclide transport is appropriate because radionuclides are expected to be in such low concentrations that they do not significantly alter the overall chemistry. The entire modelling flowchart was coded into a numerical framework denoted as iFM (interface to MARFA).

1.2 Objective and scope

The objective of this work is to demonstrate how the dynamic K_d approach can support radionuclide transport calculations carried out in the context of a safety assessment study. We aim at showing here the advantage of the dynamic K_d approach in terms of reduction of the degree of conservatism and increase of realism.

The dynamic K_d approach has been applied to assess nickel and molybdenum transport at the Laxemar site utilized for the evaluation of a proposed repository concept for SFL (SE-SFL). The main objective of the work is to analyse the implications that changing chemical conditions (computed by the ConnectFlow regional model) have on the transport and retention of these two radionuclides.

The report is structured as follows:

- The methodological approach is described in Chapter 2.

- The computed background geochemical conditions are thoroughly analysed in Chapter 3, whereas the geochemical conceptual model for nickel sorption is presented in Chapter 4.

- A method to anchor nickel K_d values computed by iFM to lab-derived data is described in Section 4.2.

- The results of nickel transport calculations are summarised in Sections 4.3 to 4.5, respectively.

- Chapter 5 is focused on the evaluation of molybdenum sorption. This section includes the molybdenum sorption model and the related dynamic K_d based MARFA calculations.

- Chapter 6 wraps up the report with summary and conclusions.

- In Appendix A, details of the new iFM version SPC (steady-pathway ConnectFlow) are provided whereas Appendix B provides details about a new analytical solution for radionuclide transport in dual porosity media with changing chemical conditions. This analytical solution is intended to be a benchmark for future applications of the dynamic K_d approach.

2   Methodological approach

The radionuclide transport calculations outlined in this report are carried out using the MARFA version denoted as SP (*static pathway* version) and the trajectories used in the simulations were computed using the ConnectFlow repository-scale model (Joyce et al. 2019; see Figure 2-1). The evolution of background geochemistry was instead simulated using the ConnectFlow regional-scale model (Figure 2-2), which spans a much larger area (400 km², approximately) and is discretised with much coarser elements.

From the above paragraph it is evident that a conceptual problem exists: how can regional-scale-computed background geochemistry be accommodated into repository-scale radionuclide transport calculations? This issue was addressed by mapping, with linear interpolation, the results of background geochemistry onto each considered trajectory segment. The mapped values of background geochemistry were then retrieved by iFM that was used to perform chemical batch calculations and provided the suitable files to be used in the final MARFA runs. A flowchart of the methodological approach is shown in Figure 2-3.

The interpolation of background geochemistry onto the considered set of streamlines has practical implications, as the change in background geochemistry actually "seen" by each streamline is much smoother than what one would expect when using a typical streamtube approach (see for instance the results of Section 4.5).

All the MARFA calculations have been carried out using version 4.0, except for the calculations of Section 4.4 that have been performed using version 4.2 dev.

It is worthwhile mentioning that at the time of starting these modelling activities, the iFM code did not include the capability of retrieving geochemistry from ConnectFlow. Thus, a customised branch version of iFM was developed. Details of this version, denoted as iFM SPC, are provided in Appendix A.
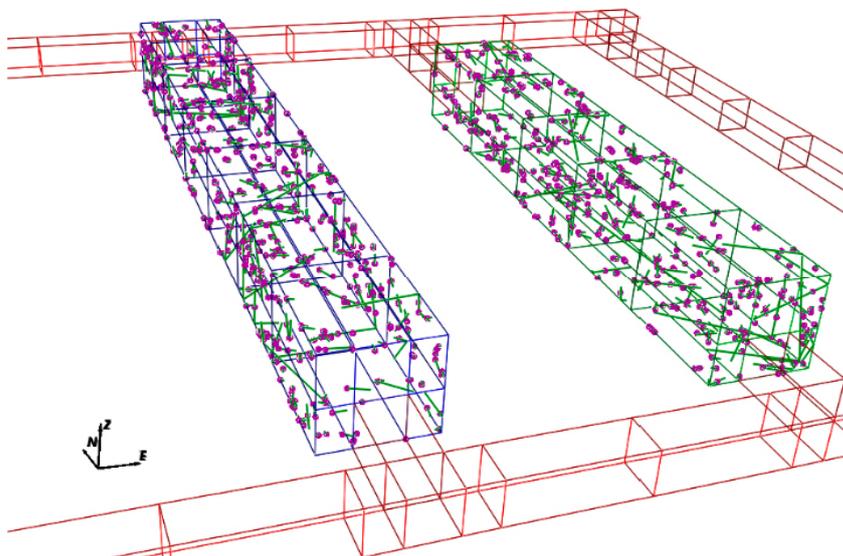

Figure 2-1. *ConnectFlow repository-scale model: detail of the injection location (figure based on the results of Joyce et al. 2019).*
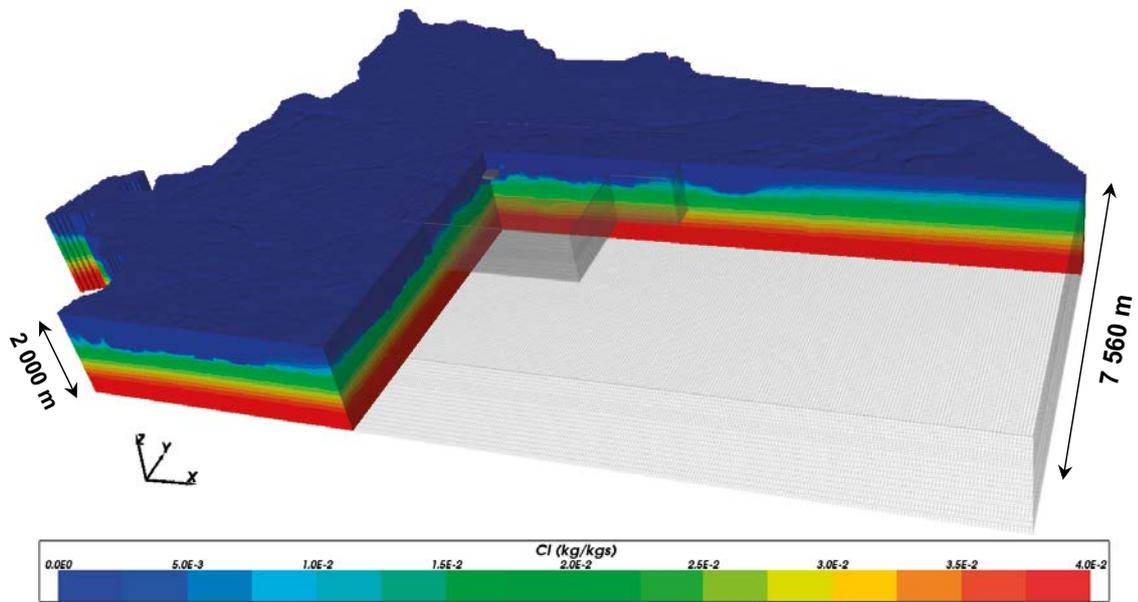
Figure 2-2. ConnectFlow regional-scale model: chloride concentration computed at 2000 AD (figure based on the results of Joyce et al. 2019).
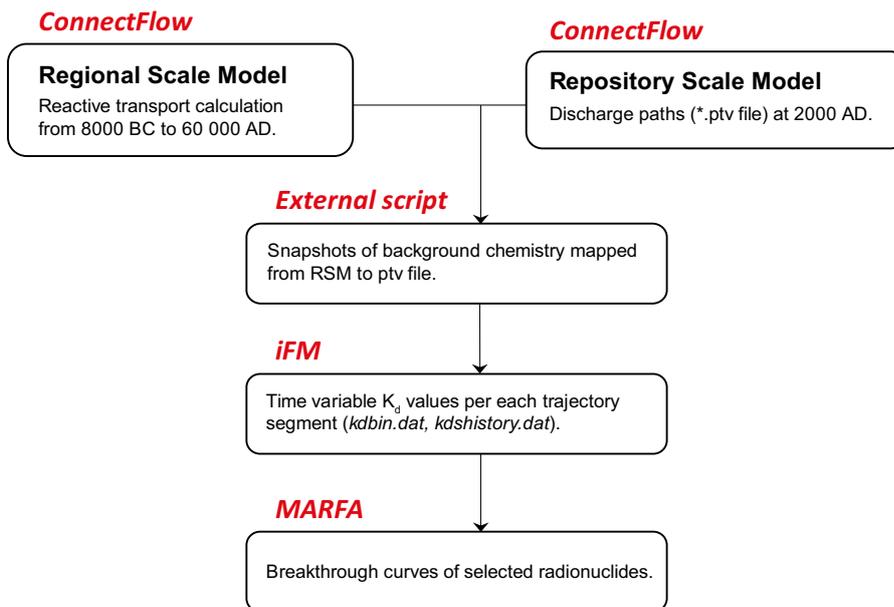

Figure 2-3. Flowchart showing the methodological approach used in the dynamic K_d calculations.

3 Analysis of background geochemistry

The update of K_d values was done considering four different temporal snapshots: 2000 AD (i.e. present conditions), 5000 AD, 20 000 AD and 60 000 AD.

First, the computed values of major geochemistry were visually analysed in the regional-scale domain. The evolution of chloride mass fraction and pe is shown in Figure 3-1 to Figure 3-4 (other species and parameters are not shown here for the sake of brevity). These figures provide a general overview of the regional chemical patterns (e.g. the water stratification, with salinity increasing with depth) but are not useful to infer relevant information about the evolution of chemistry at repository-scale. Thus, chloride evolution in the repository volume is shown in Figure 3-5. From this figure, it is evident that salinity is gradually decreasing as a result of infiltration processes. This is further confirmed by Figure 3-6, which shows box-whisker plots for the evolution of salinity (total dissolved solids, TDS) at repository depth. In the same figure analogous results, computed for the Laxemar model by Gimeno et al. (2010) using a different modelling approach, are shown. It is evident that the SE-SFL hydrochemical calculations provide significantly lower estimates of salinity. We will see in Section 4.2 and Section 4.3 that this has an important impact on radionuclide retention. It is worthwhile noting that an exhaustive critical comparison between these two models is out of the scope of this work. We want to simply point out here that the diluted conditions observed in the ConnectFlow model have a significant impact on the retention processes that are modelled hereafter.
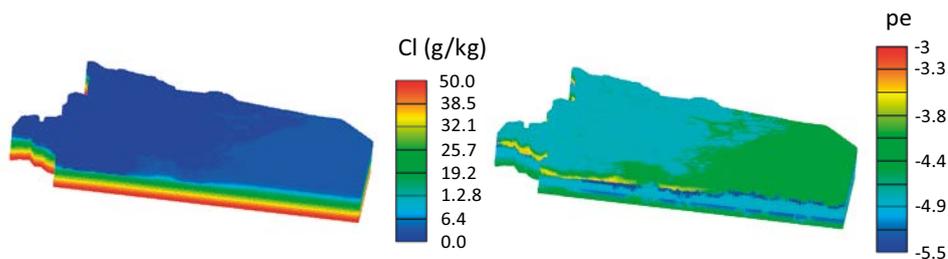
Figure 3-1. *Chloride mass fraction (left) and pe (right) computed by the regional-scale model at time 2000 AD. The vertical extension of the regional-scale model is also indicated. Results taken from Joyce et al. (2019).*
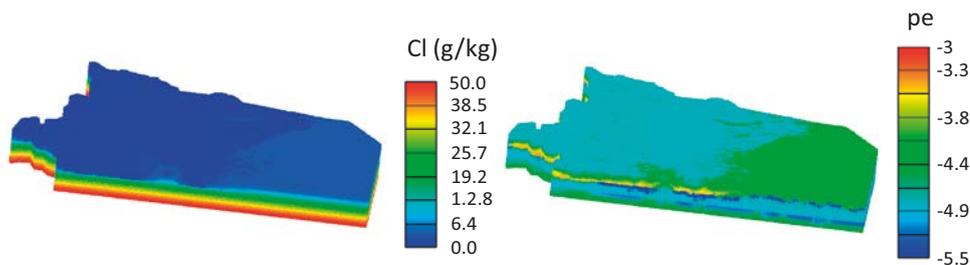
Figure 3-2. *Chloride mass fraction (left) and pe (right) computed by the regional-scale model at time 5000 AD. Results taken from Joyce et al. (2019).*
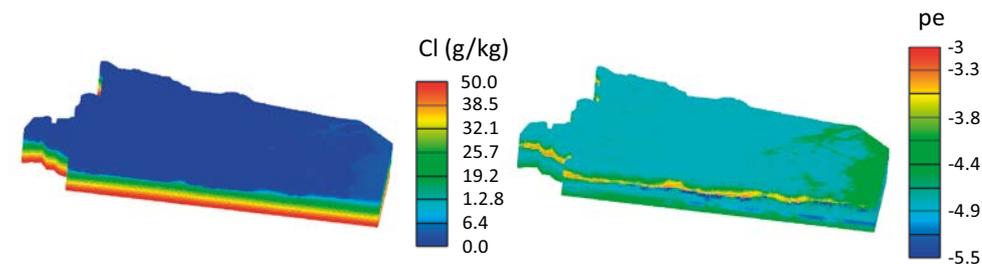
Figure 3-3. *Chloride mass fraction (left) and pe (right) computed by the regional-scale model at time 20 000 AD. Results taken from Joyce et al. (2019).*
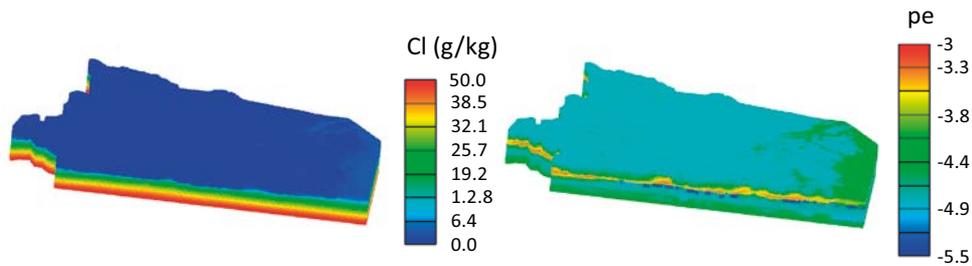
Figure 3-4. *Chloride mass fraction (left) and pe (right) computed by the regional-scale model at time 60 000 AD. Results taken from Joyce et al. (2019).*
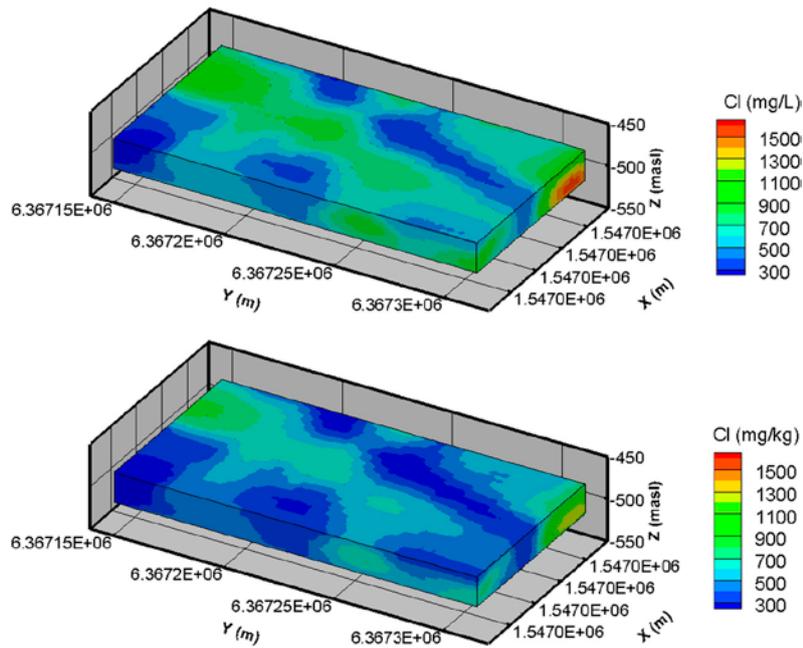
Figure 3-5. *Chloride mass fraction at repository depth at 2000 AD (top) and 5000 AD (bottom). Results taken from Joyce et al. (2019).*
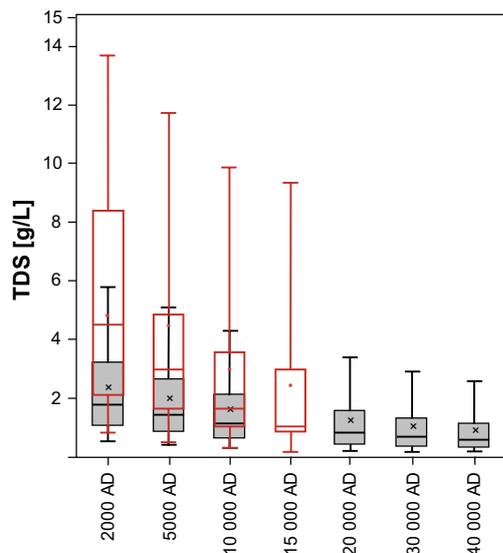
Figure 3-6. *Box-whisker plot (grey shaded boxes) showing the evolution of TDS at repository depth (modified from Joyce et al. 2019). The red unfilled boxes are the results (TDS concentration) computed at repository depth for the Laxemar site by Gimeno et al. (2010).*

4 Assessing nickel transport and sorption using a dynamic K_d approach

4.1 Conceptual model for nickel sorption

Previous studies have provided mineralogical descriptions of the rock matrix at Laxemar. Drake and Tullborg (2009) pointed out that "*apart from the higher quartz content, the Ävrö granodiorite has somewhat higher contents of K-feldspar but lower contents of biotite, amphibole, plagioclase and opaques than the Ävrö quartz monzodiorite*".

Biotite is a particularly important sorbing phase (Crawford 2013). However, to the knowledge of the authors, no specific model for nickel sorption onto biotite exists. Thus, considering that biotite's crystallography is similar to illite, we used the model for sorption of nickel onto biotite (Bradbury and Baeyens 2009) as a proxy for nickel sorption in the granite. A similar approach was used by Crawford (2013) to evaluate K_d values to be used for the SR-PSU project. The list of surface complexation, cation exchange and protolysis reactions included in the model is listed in Table 4-1.

Table 4-1. Mass action equations and the associated surface complexation, cation exchange and protolysis constants (Bradbury and Baeyens 2009).

| Surface complexation on strong sites	log K_{sc}
$\equiv S^S OH + Ni^{2+} \leftrightarrow \equiv S^S ONi^+ + H^+$	0.7
$\equiv S^S OH + Ni^{2+} + H_2O \leftrightarrow \equiv S^S NiOH^0 + 2H^+$	−8.2
$\equiv S^S OH + Ni^{2+} + 2H_2O \leftrightarrow \equiv S^S ONi(OH)_2^- + 3H^+$	−17.3

Cation exchange on planar sites	log K_c
$2NaX + Ni^{2+} = NiX_2 + 2Na^+$	1.1

Protonation/deprotonation reactions	log K
$\equiv S^S OH + H^+ \leftrightarrow S^S OH_2^+$	4.0
$\equiv S^S OH \leftrightarrow S^S O^- + H^+$	−6.2

4.2 Anchoring the conceptual model to lab-derived data

One of the biggest uncertainties of mechanistic reactive transport models is the availability of sorption sites (i.e. the density of sorption sites, CES). This is strongly related to the underlying mineral phases, which in turn are heterogeneously distributed. Thus, a prior task of this modelling activity has been to anchor the number of sorption sites to the available lab-derived nickel distribution coefficients.

In the work of Bradbury and Baeyens (2009), a ratio of $\frac{\equiv S^S OH}{X} = 8.9 \times 10^{-3}$ is provided (note that X is the number of exchange sites, in eq/mol). Keeping this ratio fixed, the amount of amphoteric edge sites and cation exchange sites has been calibrated to fit the nickel distribution coefficient (central value) provided by Crawford (2013); i.e. $K_d = 7.4 \times 10^{-4}$ m^3/Kg. This value was computed in the framework of the SFR-PSU safety assessment project and was assumed to be representative of temperate conditions. Thus, mechanistic PHREEQC calculations were carried out, where nickel, in trace concentration, was added to the temperate saline water defined for the SR-PSU project (Table 4-2). The sorption model explained in Chapter 1 was included in the calculations, which were performed using the SKB thermodynamic database (Duro et al. 2006), and the total number of sites was manually calibrated to fit the target K_d value mentioned before.

The resulting concentration of sorption sites was estimated to be $\equiv S^S OH = 4.5 \times 10^{-4}$ mol/L and the concentration of cation exchange sites $X = 5.1 \times 10^{-2}$ mol/L. The contribution to the overall sorption of the individual Ni sorption species is shown in Figure 4-1. From the figure it is evident that, given this background conditions, surface complexation, and in particular the nickel species $\equiv S^S ONi^+$, is dominant.
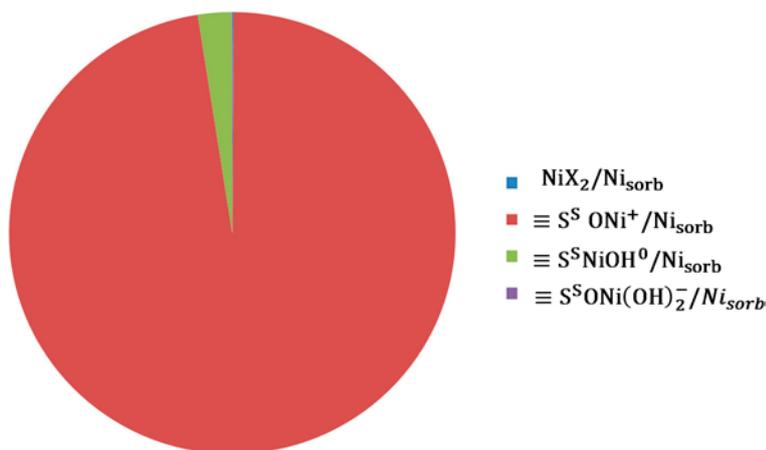
Figure 4-1. *Contributions to the overall sorption of the individual Ni surface species.*

Legend:
- NiX_2/Ni_{sorb}
- $\equiv S^S ONi^+/Ni_{sorb}$
- $\equiv S^S NiOH^0/Ni_{sorb}$
- $\equiv S^S ONi(OH)_2^-/Ni_{sorb}$

Table 4-2. Composition of the temperate saline water used in the SR-PSU safety assessment (Auqué et al. 2013).

	SR-PSU Temperate saline
pH	7.3
Eh (mV)	−225
Cl^- (mg/L)	3 500
SO_4^{2-} (mg/L)	350
HCO_3^- (mg/L)	90
Na^+ (mg/L)	1 500
K^+ (mg/L)	20
Ca^{2+} (mg/L)	600
Mg^{2+} (mg/L)	150
SiO_2 (mg/L)	11

4.3 Results

4.3.1 Analysis of K_d values along a single trajectory

To understand the details and implications of changes in background geochemical conditions, a single trajectory has been extracted and thoroughly analysed.

The distribution of chloride concentration, pH and pe at time 2000 AD along the selected trajectory is shown in Figure 4-2. A significant impact of altered meteoric water is observed close to the repository volume, where chloride concentration is far below 1 000 mg/Kg. In this area, higher pH values are also observed as a result of mineral buffering processes (calcite dissolution). Diluted groundwater is also observed in the shallow part of the domain (i.e. close to the discharge area).

iFM has been used to compute the K_d values along the selected trajectory (Figure 4-3 and Figure 4-4). Close to the repository volume and close to the surface the computed K_d values are higher that the upper bound provided in Crawford (2013) due to the relatively diluted groundwater composition, which decreases significantly the competition for sorption sites. The (negative) correlation between K_d and chloride concentration is also shown in Figure 4-5. A positive correlation is observed between K_d and pH, although the range of pH variation is quite modest.

The contribution of each nickel surface species computed at time 2000 AD and at three different points in the trajectory is shown in Figure 4-6. Close to the repository and the surface (i.e. where groundwater is significantly diluted) cation exchange becomes more important and K_d values are high, while in the middle of the trajectory the resulting distribution coefficient is close to the target value defined in Section 4.2.
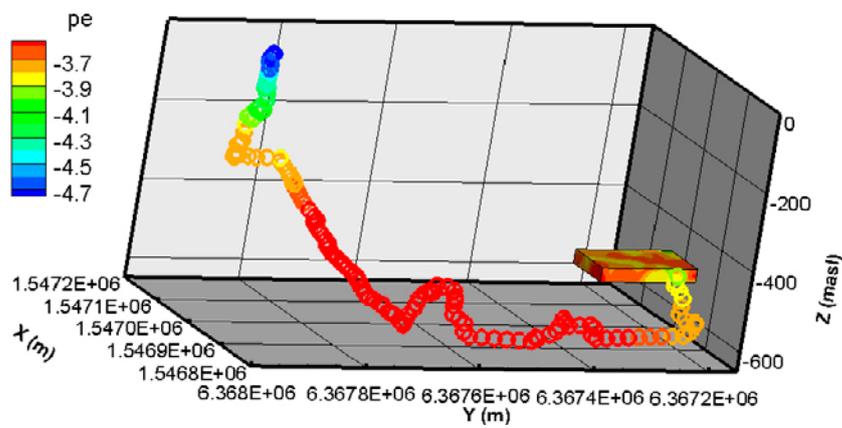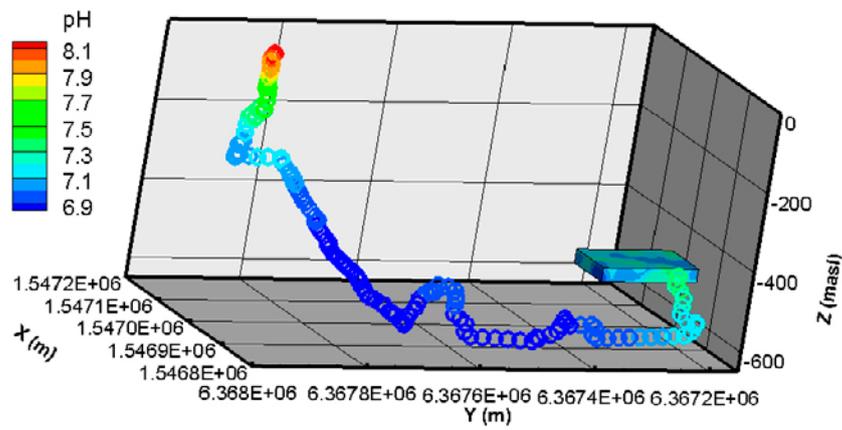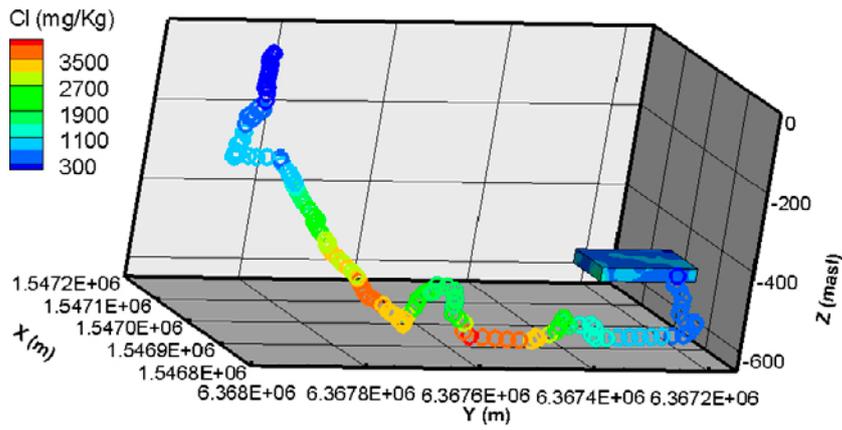
Figure 4-2. *(top) chloride, (middle) pH and (bottom) pe computed by the ConnectFlow regional scale model at 2000 AD and mapped along a single trajectory. Results taken from Joyce et al. (2019).*
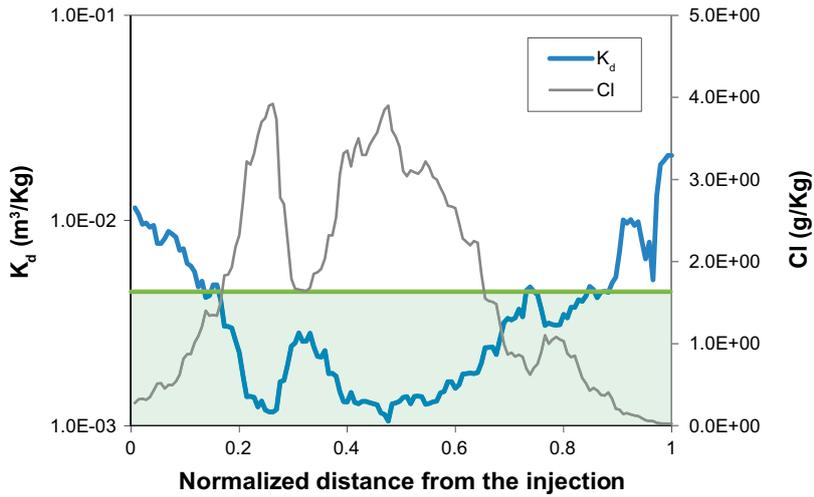
Figure 4-3. K_d *values (bold line) and chloride concentration versus normalised distance from the injection along the selected trajectory at time 2000 AD. The shaded area indicates the range of K_d provided by Crawford (2013).*
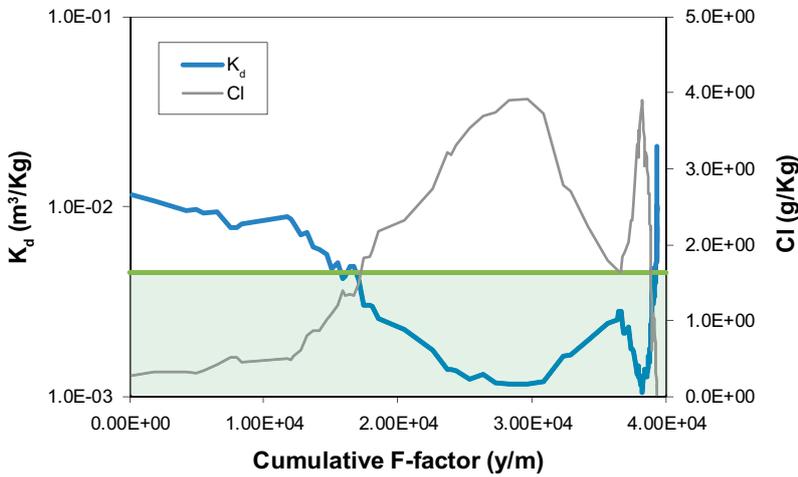
Figure 4-4. K_d *values (bold line) and chloride concentration versus cumulative F-factor along the selected trajectory at time 2000 AD. The shaded area indicates the range of K_d provided by Crawford (2013).*
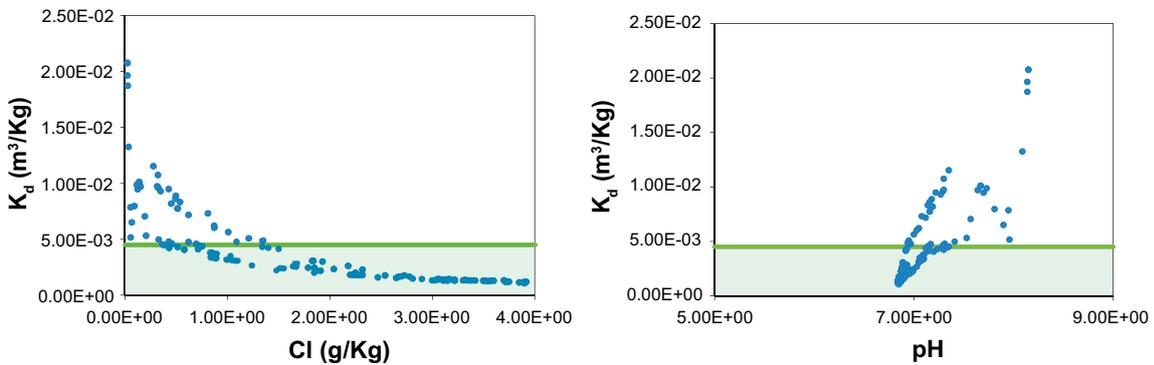
Figure 4-5. *(left) K_d values versus chloride concentration and (right) K_d values versus pH, at time 2000 AD. Each dot represents a single trajectory segment. The shaded area indicates the range of K_d provided by Crawford (2013).*
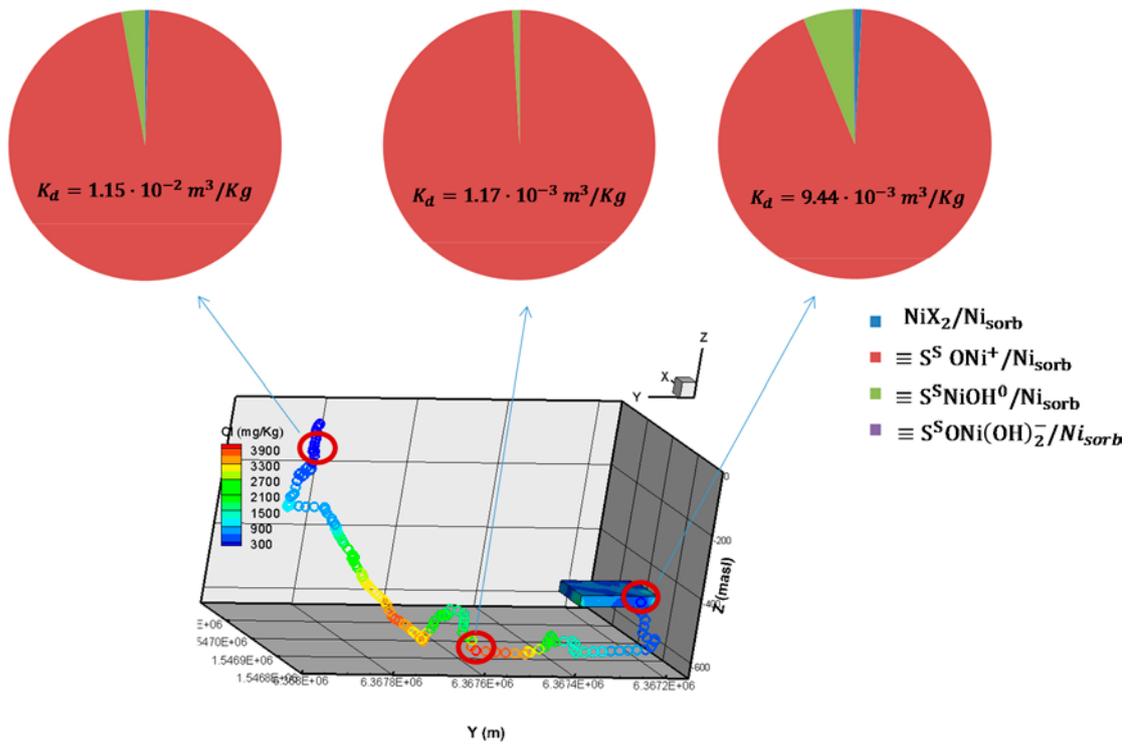
Figure 4-6. *Contributions to the overall sorption of the individual Ni surface species computed at 2000 AD at three different points along the trajectory. The resulting K_d value is also indicated.*

The temporal evolution of K_d values along the selected trajectory is shown in Figure 4-7 and Figure 4-8. Due to the progressive infiltration of meteoric water, the competition for sorption sites and the aqueous complexation reactions become less important, thus increasing the retention capacity of the system. At time 60 000 AD (i.e. the last snapshot considered in the model), the K_d values are above the range provided by Crawford (2013) along the entire trajectory.
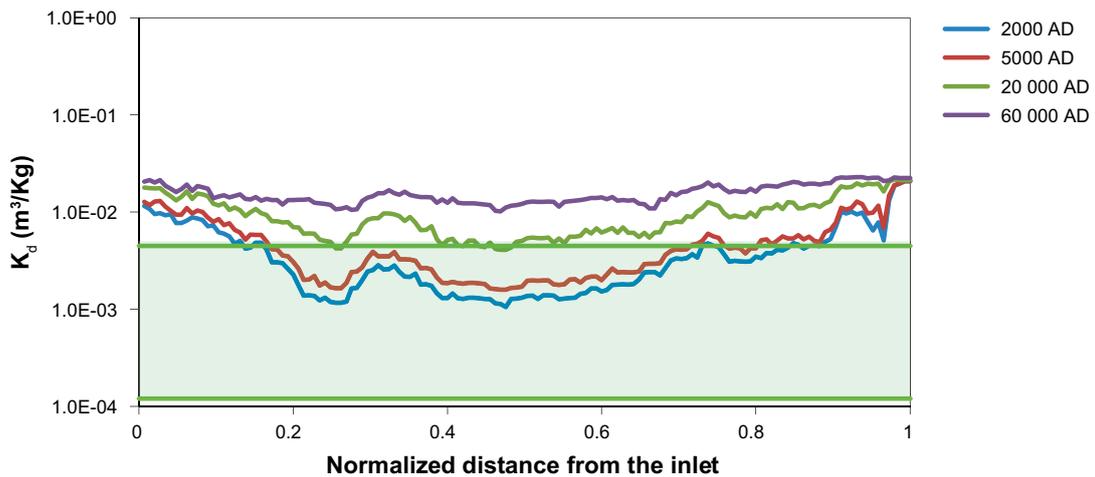
Figure 4-7. *K_d values versus normalised distance from the inlet computed by iFM along the selected trajectory at different times.*
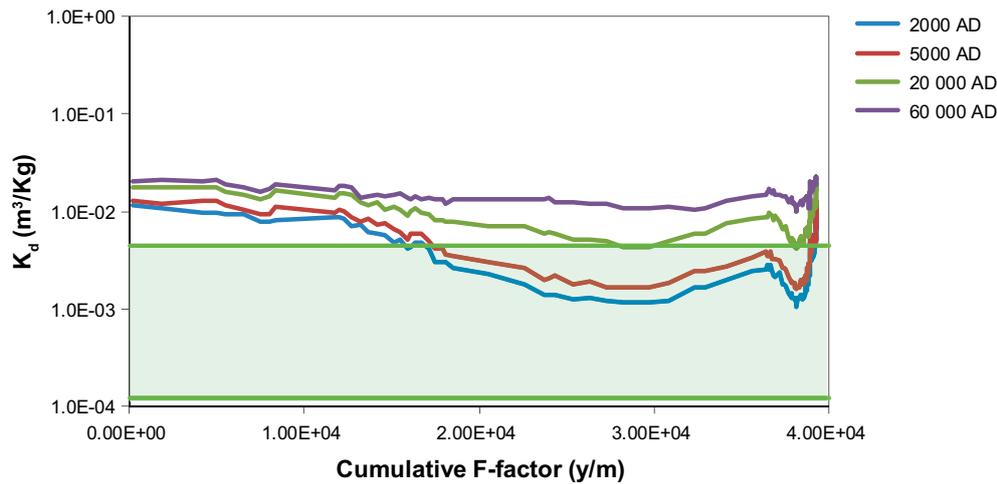
Figure 4-8. K_d values versus cumulative F-factor computed by iFM along the selected trajectory at different times.

4.3.2 MARFA calculations with dynamic K_d

The radionuclide transport calculations (MARFA SP calculations) were carried out along the ensemble of trajectories starting from BHA (Figure 4-9). The release functions for Nickel-59 (1.01×10^5 y half-life) and Nickel-63 (100 y half-life) were obtained from results of Ecolego near-field calculations (Figure 4-10).

Three independent set of calculations were performed:

- K_d *constant calculations* => constant K_d values for all the trajectory segments (7.4×10^{-4} m^3/Kg).

- K_d *spatially variable calculations* => spatially variables K_d values computed by iFM using background geochemistry computed at 2000 AD. No update of K_d values.

- *Dynamic K_d calculations* => spatially variables K_d values computed by iFM (2000 AD) and updated at 5000 AD, 20 000 AD and 60 000 AD.
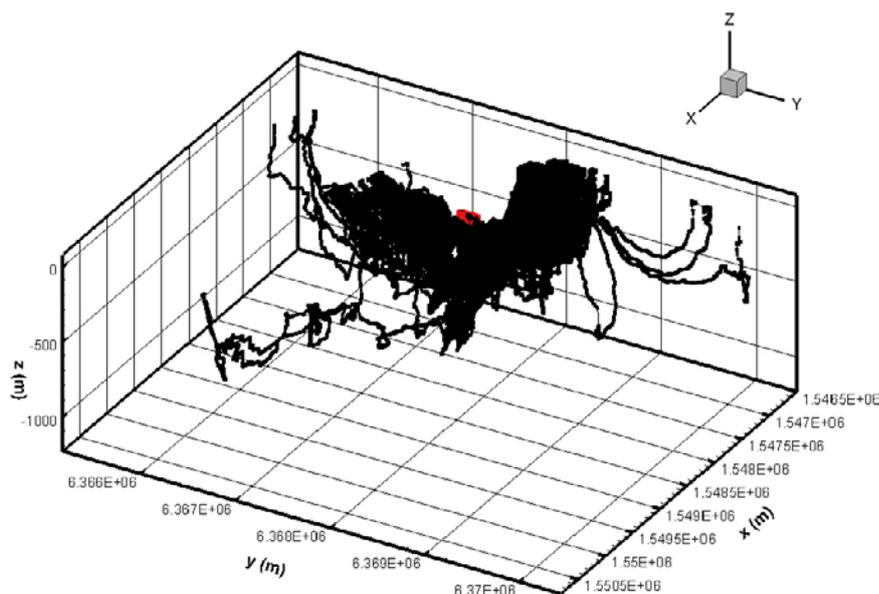
Figure 4-9. 2 437 trajectories released at BHA and used for the MARFA calculations (unsuccessful trajectories, i.e. trajectories that did not reach the boundary, have been removed). The trajectories are computed using the velocity field at 2000 AD. The red dots indicate the release points.
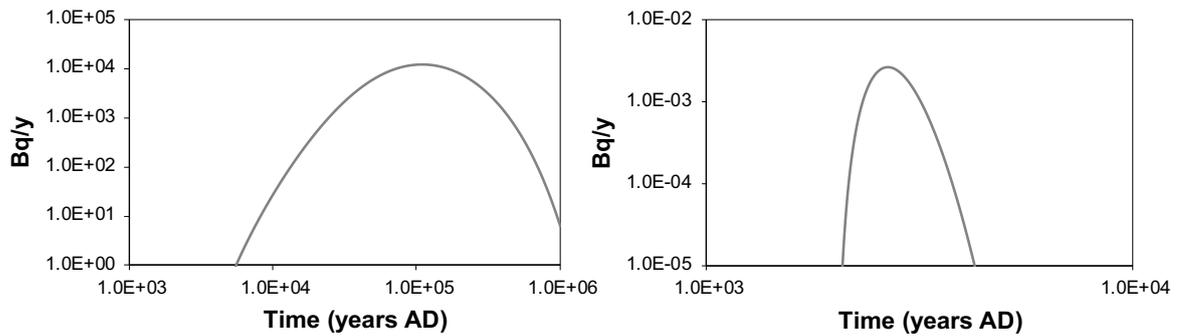
Figure 4-10. Release function of (left) Ni-59 and (right) Ni-63 at BHA as computed by Ecolego near-field calculations.

The breakthrough curves for Ni-59 are shown in Figure 4-11. It can be noticed that by simply defining initially heterogeneous conditions (i.e. K_d values computed at 2000 AD but no update in time) the retention capacity of the system is significantly increased. When K_d values are updated in time, the observed concentration is further decreased, with an observed maximum concentration which is less than half of the value observed in the calculations with constant K_d. It is worthwhile noting that the breakthrough curve computed with the dynamic K_d approach has been reconstructed using a higher gamma value (i.e. lower bandwidth) to avoid any smoothing effect that could have masked the effect of updating K_d values. This higher gamma value leads to more statistical noise, which explains the small oscillations of the breakthrough curve.

Due to its short half-life ($\approx$100 y), Ni-63 is not affected by changes in geochemical conditions. Yet, initial geochemical conditions strongly affect the transport of this radioisotope. In fact, neglecting the initial heterogeneous distribution of major geochemistry leads to a significant underestimation of the retention capacity of the system. Figure 4-13 shows the cumulative mass of Ni-63 for both the constant K_d calculation and the spatially variable K_d. The difference in mass is related to decay processes. With higher K_d values (dynamic K_d approach) retention times are also higher and, thus, more mass is decayed and less mass is observed at the outlet. The similar shape of the instantaneous breakthrough curves is related to the source function, which has a rising limb that peaks at t = 1 000 y, approximately.
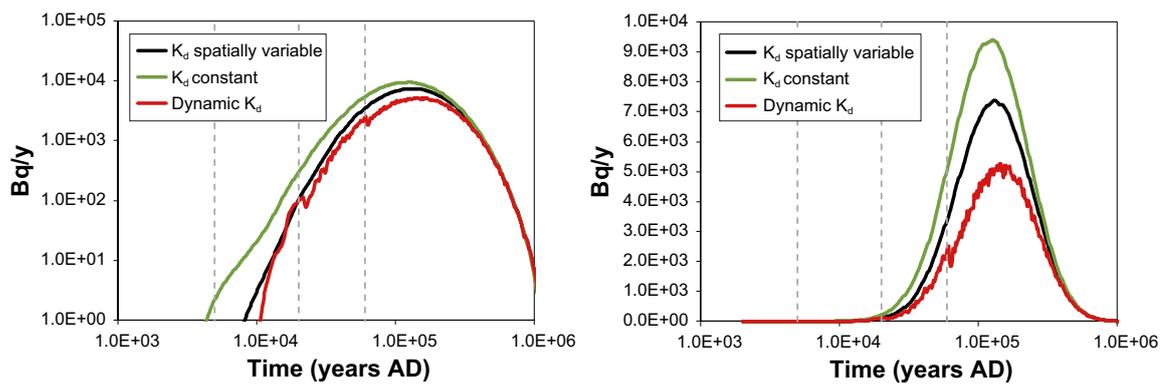
Figure 4-11. Breakthrough curves of Ni-59 (left: log-log scale; right: semi-log scale) computed using K_d constant, K_d spatially variable and the dynamic K_d approach. Vertical dashed lines indicate the time of the update of K_d values.
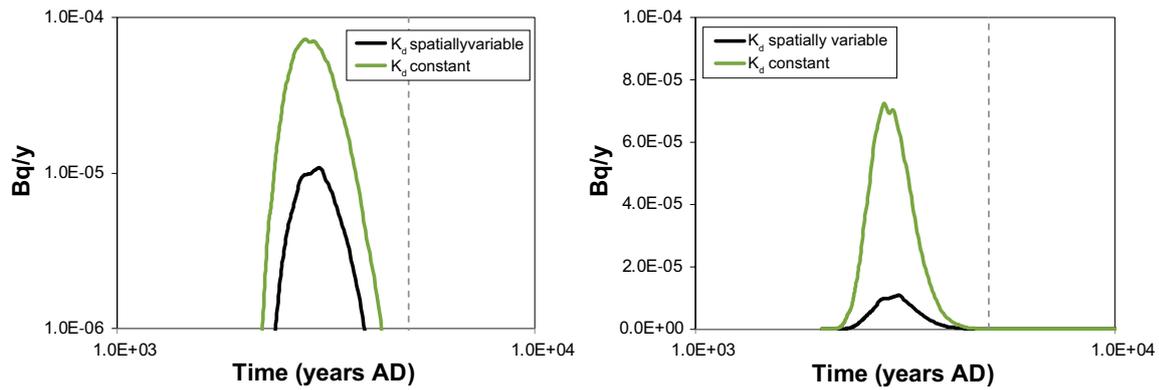
Figure 4-12. *Breakthrough curves of Ni-63 (left: log-log scale; right: semi-log scale) computed using K_d constant, K_d spatially variable and the dynamic K_d approach. Vertical dashed lines indicate the time of the update of K_d values.*
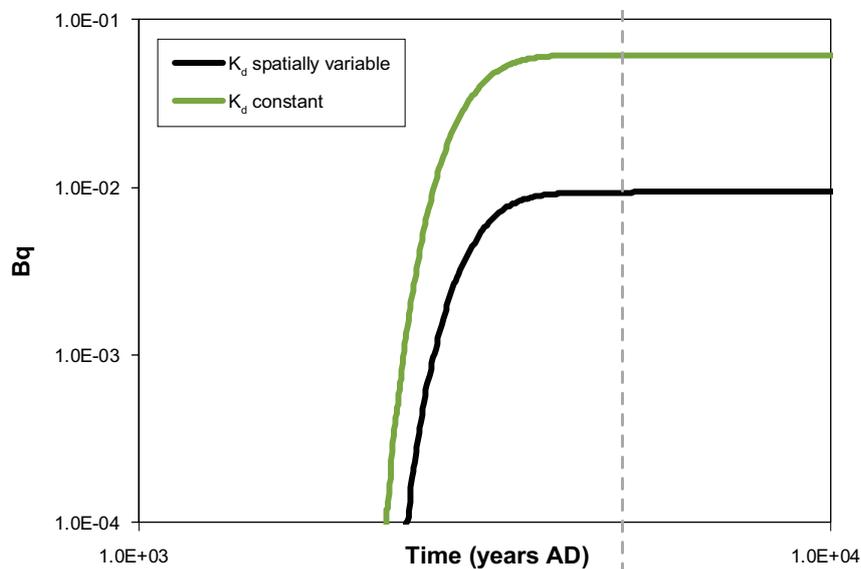
Figure 4-13. *Cumulative mass of Ni-63 computed using K_d constant, K_d spatially variable and the dynamic K_d approach. Vertical dashed lines indicate the time of the update of K_d values.*

4.4 Calculations with the MARFA NR version

This section summarises the different steps required to carry out nickel dynamic K_d calculations with the NR version of MARFA.

4.4.1 Preparation of the MARFA input files

The Marfa input files preparation is illustrated in Figure 4-14.
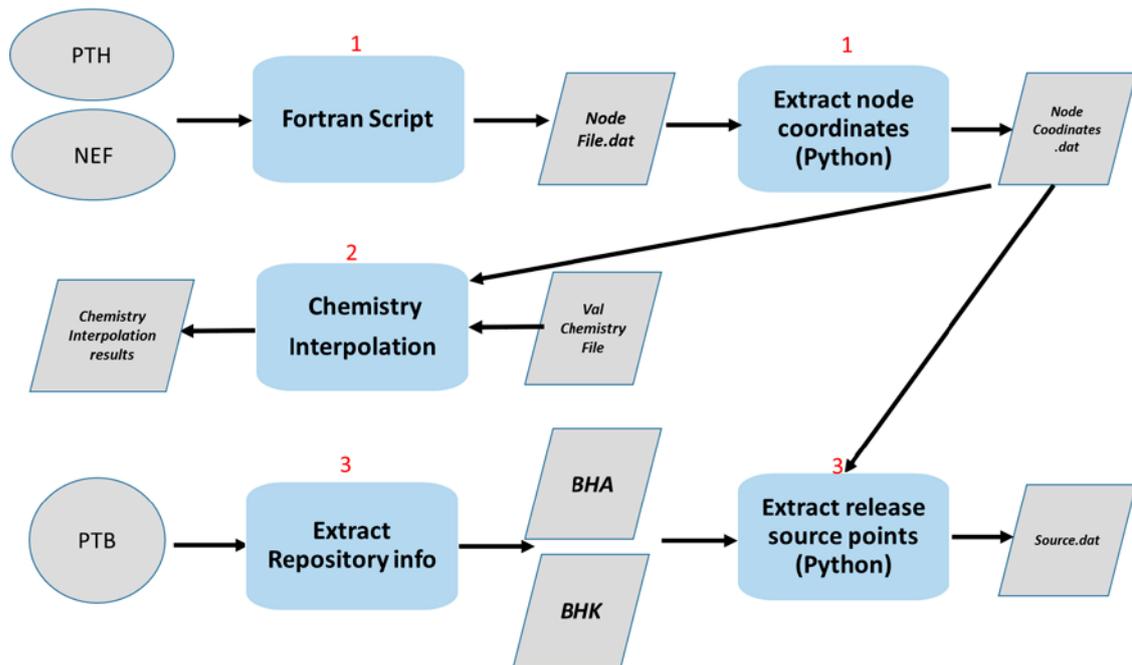
Figure 4-14. Marfa input files preparation flowchart.

Step (1) Reading PTH/NEF to write NodeFile.dat: Using a helper application provided in Marfa source code repository, the Connect Flow outputs including (*.PTH and *.NEF) files are read in order to write a node file with format suitable for Marfa. As a complementary step the coordinates of all the nodes in NodeFile.dat are separately written to a secondary file (NodeCoordinates.dat). This file is later used when interpolating chemistry for each node.

Step (2) Interpolating Chemistry for all nodes in Node Network (ptv files): At this step the chemistry values for the node network (step 1) are interpolated from the chemistry input files delivered by Amec for times 2000 AD, 5000 AD, 20 000 AD and 60 000 AD.

The following methods have been used for interpolation.

1. Scipy.interpolate: Python sub-package that includes functions and classes for objects used in interpolation.
2. Scikit-learn: Machine Learning library in python built based on Numpy, Scipy and Matplotlib.
3. SGeMS: The Stanford Geostatistical Modelling Software (SGeMS) is an open-source computer package for solving problems involving spatially related variables.
4. Tecplot: post processing tool to analyse data.

Method of bullet point nr.1 was used in the actual calculations, whereas the other methods were used to cross-check the results of the interpolation.

Step (3) Converting PTB to get injection file: Using the *.PTB file, a list of node numbers which are the release injection points from the two repositories BHA and BHK have been extracted to prepare SOURCE.DAT input for Marfa.

In Figure 4-15, two-dimensional X-Y plane of the BHA and BHK repositories with the injection locations are represented.
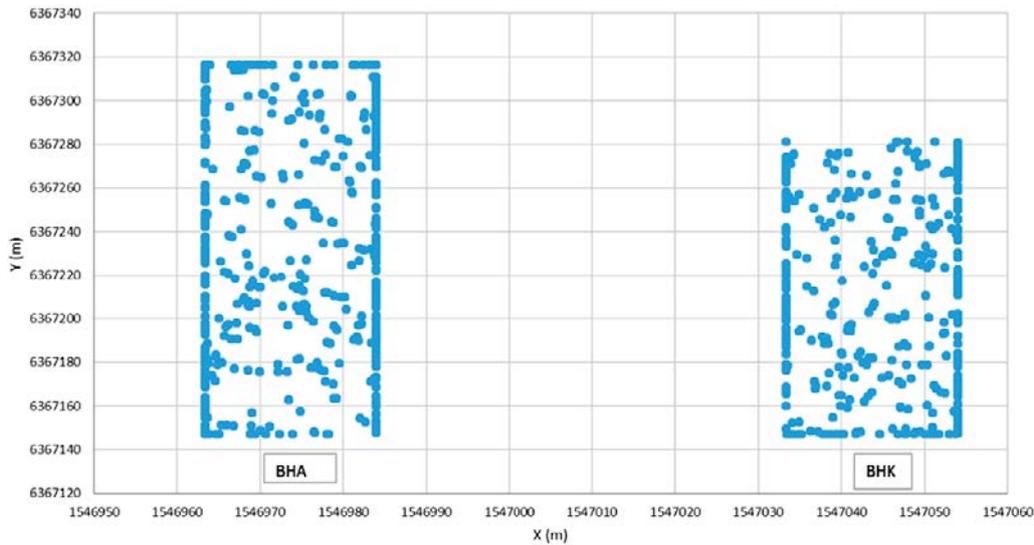
Figure 4-15. Injection point locations in two dimensional x-y plane, repositories BHA (left) and BHK (right) are shown.

4.4.2   Model set-up and results

The node network data file generated by ConnectFlow consists of 105 373,637 nodes. As the current version of iFM is not parallelised, running the code over this huge data file implies computing more than one hundred million sequential PHREEQC calculations, which means that iFM would run for more than ten days for each temporal snapshot. Thus, given the demonstrative purpose of these calculations, an alternative option was adopted here; i.e. chloride concentration is used as a marker for the evolution of background geochemistry. More specifically, the K_d vs. chloride concentration values computed for a single trajectory at 2000 AD (Figure 4-5) are used to infer a regression line (Figure 4-16), which is based on the following equation:

$$K_d = -5 \times 10^{-3} \log_{10}(Cl) + 4.3 \times 10^{-3}$$
Equation 4-1

A modified version of iFM is then run using the ptv files described in Section 4.4.1 as input and Equation 4-1 is used to compute the K_d values for each node of the routing file and for each considered time.
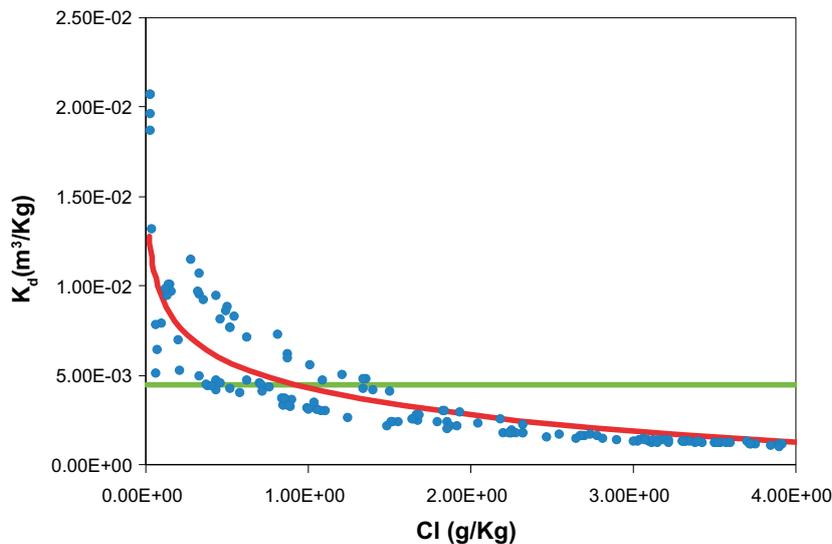
Figure 4-16. K_d values versus chloride concentration for a single trajectory computed at time 2000 AD. Each dot represents a single trajectory segment. The green line indicates the upper range of K_d provided by Crawford (2013). The red line is the regression line used in the iFM_NR calculations.

In this numerical exercise Ni-59 is considered and, unlike the calculations of Section 4.2 that were focused on BHA only, here the release from both BHA and BHK is considered (Figure 4-17). Given the shape of the BHK source function, with a clear peak at around 2×10^5 year the time frame of the calculation has been extended to 1×10^6 years.

K_d values computed for 1 000 arbitrarily selected nodes at 2000 AD, 5000 AD and 20 000 AD are shown in Figure 4-18. Note that it is difficult to establish a direct relationship with the evolution of K_d observed along a single trajectory (Figure 4-7), as these nodes are randomly picked in different parts of the domain, which might in turn be characterised by significantly different geochemical conditions.

The instantaneous and cumulative breakthrough curve of Ni-59 is shown in Figure 4-19. Similarly to what already observed in Section 4.3, when the temporal evolution of K_d values is taken into account, a reduction in the cumulative mass discharge is also observed. However, compared to the SP calculations, this reduction is here more modest (~10 %) probably due to the different discharge patterns (and, consequently, different hydrochemical zones) "sampled" by the particle released at BHK.
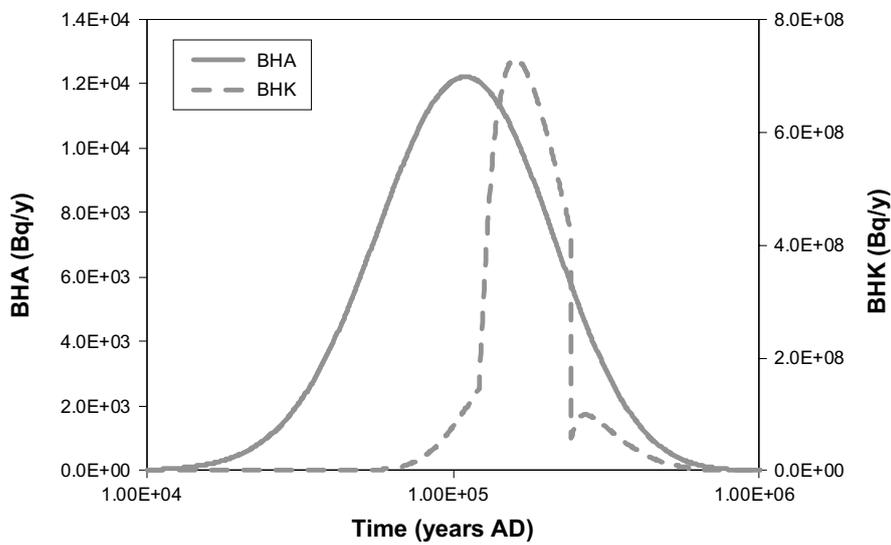
Figure 4-17. *Release functions of Ni-59 for BHA (continuous line and left axis) and BHK (dashed line and right axis).*
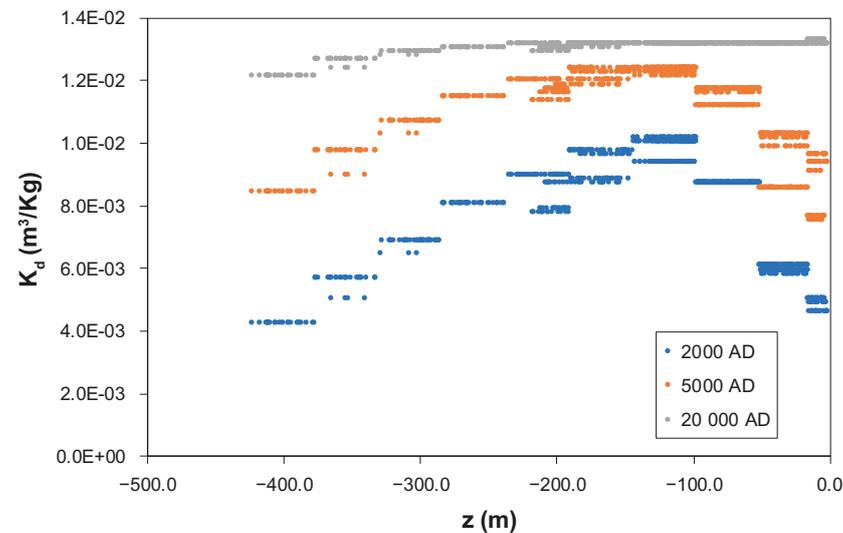
Figure 4-18. *K_d values vs. depth for 1 000 arbitrarily selected nodes computed at 2000 AD, 5000 AD and 20 000 AD.*
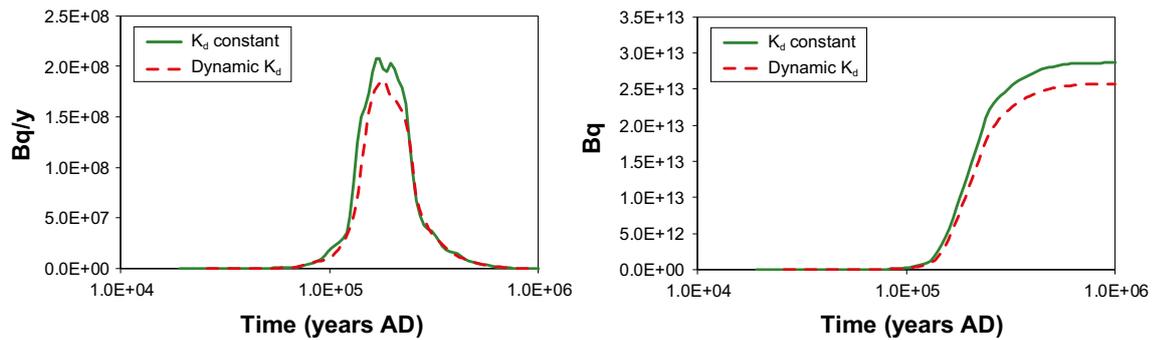
Figure 4-19. Instantaneous (left) and cumulative (right) breakthrough curves of Ni-59 computed using K_d constant, and the dynamic K_d approach.

It is worthwhile mentioning here that iFM is continuously under-going improvements and maintenance. One of the pending developments is to parallelise the execution of the PHREEQC 0D calculations. This new capability will allow complex and big model such as that discussed in this section, to be run in powerful workstations without the need for employing any simplifying assumption.

4.5 Scoping calculations for a glacial period

An additional task performed in the framework of the SE-SFL safety evaluation project has been to analyse the possible application of the dynamic K_d approach to the simulation of radionuclide transport during a glacial period. Considering that the hydrogeological models of SE-SFL did not include any simulation of flow periods with periglacial and glacial conditions, this objective was achieved by means of simplified reactive transport calculations.

The conceptual model, which is illustrated in Figure 4-20, considers a single recharge-discharge pathway that is assumed to be fixed in time. The travel time for the recharge pathway is 8 y, while in the discharge pathway groundwater takes 135 y to "move" from the repository volume to the discharge area. Groundwater velocity is also assumed to be constant during the whole simulation time frame (Figure 4-21). The possible generation and interaction of cement plumes from the repository is not considered here. Possible changes in the flow paths induced by changes in the position of the glacial front are also neglected.
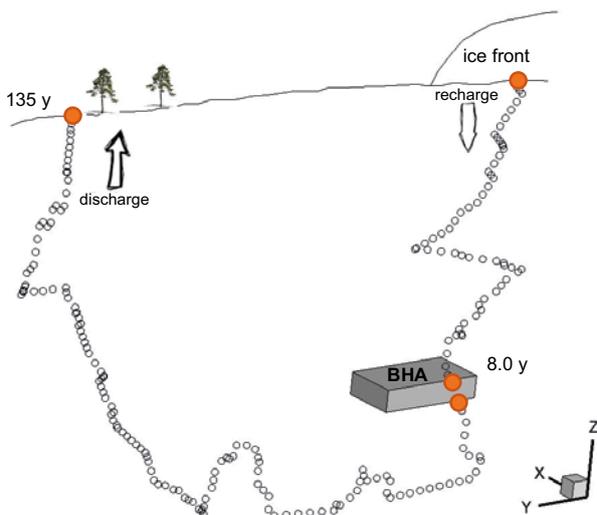
Figure 4-20. Sketch of the conceptual model used to mimic the infiltration of glacial meltwater and its influence on radionuclide transport.
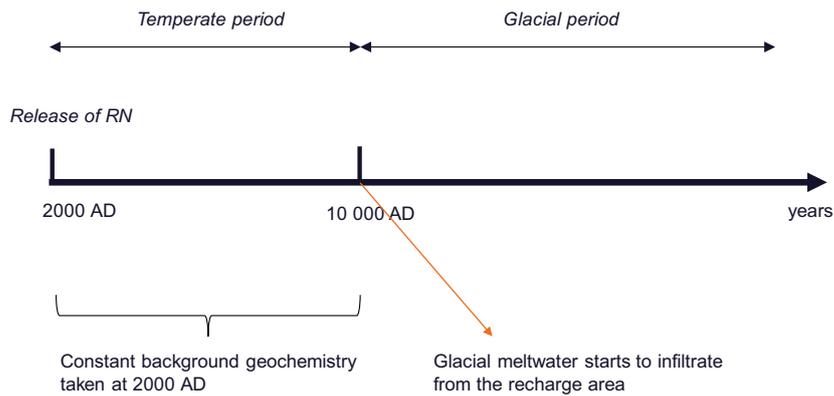
Figure 4-21. *Simulation time frame for the glacial calculations.*

FASTREACT (Trinchero et al. 2014) was used to simulate the infiltration of glacial water (Table 4-3) into the system. The glacial end-member composition listed in Salas et al. (2010) was used as boundary water (Table 4-3). The glacial melt water was equilibrated with calcite and mackinawite.

A simplification of this model is that no matrix diffusion is considered in the reactive transport calculations. This means that the geochemical conditions computed along the pathway, which represents the flowing fracture, are used to define geochemical changes in the matrix. A more elaborated model would have implied the use of the dual-approach implemented in PHREEQC.

Table 4-3. Composition of the glacial water used in the glacial calculations (Salas et al. 2010).

	Glacial Groundwater
pH	5.8
pe	15.5
Total concentrations (mol/L)	
Cl	2.0×10^{-5}
Ca	3.2×10^{-6}
Na	6.5×10^{-6}
S	5.2×10^{-7}
Mg	4.1×10^{-6}
K	3.8×10^{-6}
Fe	1.8×10^{-9}
Si	1.7×10^{-7}
C	2.6×10^{-6}

Snapshots of chloride concentration, pH and pe at the beginning of the calculation and after 50 y from the beginning of the "perturbation" (i.e. 10 050 AD) are shown in Figure 4-22 and Figure 4-23, respectively. From these figures it is evident that the penetration of glacial meltwater results in a significant dilution of the system. In the part of the pathway overtaken by the perturbation, pH increases up to values of around 10 due to the effect of calcite dissolution whereas pe decreases to more anoxic conditions as a result of the buffering effect of mackinawite.

The evolution of nickel K_d values, computed by iFM along the selected trajectory, is shown in Figure 4-24. The infiltration of glacial water leads to a significant increase of nickel retention. At time 10 143 AD (i.e. 143 y after the beginning of the perturbation) a constant K_d values equal to 2.6×10^{-1} m^3/Kg is observed along the entire trajectory. These results have been used to produce the input files used in the dynamic K_d calculations, whose results (Ni-59) are shown in Figure 4-25. From this figure it is evident that when diluted conditions propagate deep into the system, radionuclide retention increases dramatically. The net effect of this is a significant reduction of nickel mass discharge. Given its short half-life, similar calculations have not been carried out for Ni-63.
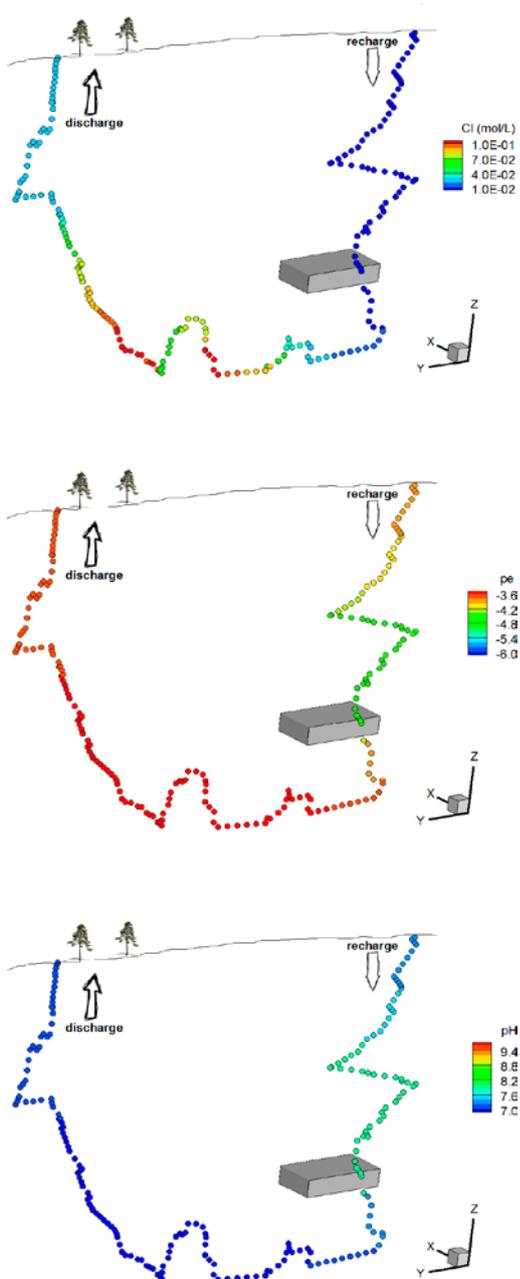
Figure 4-22. *Initial conditions (2000 AD) along the recharge-discharge pathway. From top to bottom: chloride, pe and pH.*
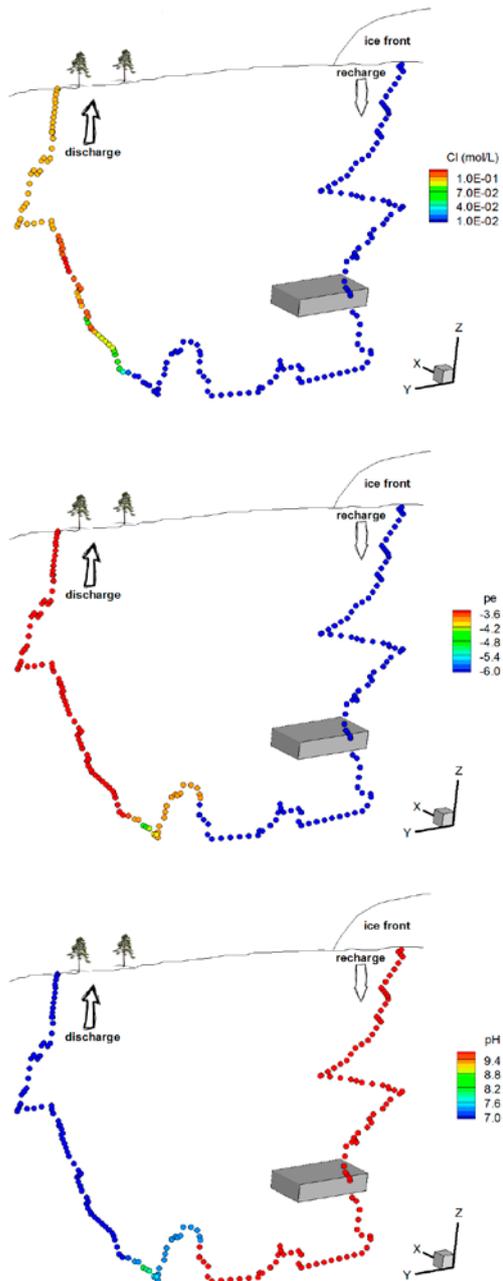
Figure 4-23. *Hydrochemical conditions computed after 50 y from the beginning of the perturbation (10050 AD) along the recharge-discharge pathway. From top to bottom: chloride, pe and pH.*
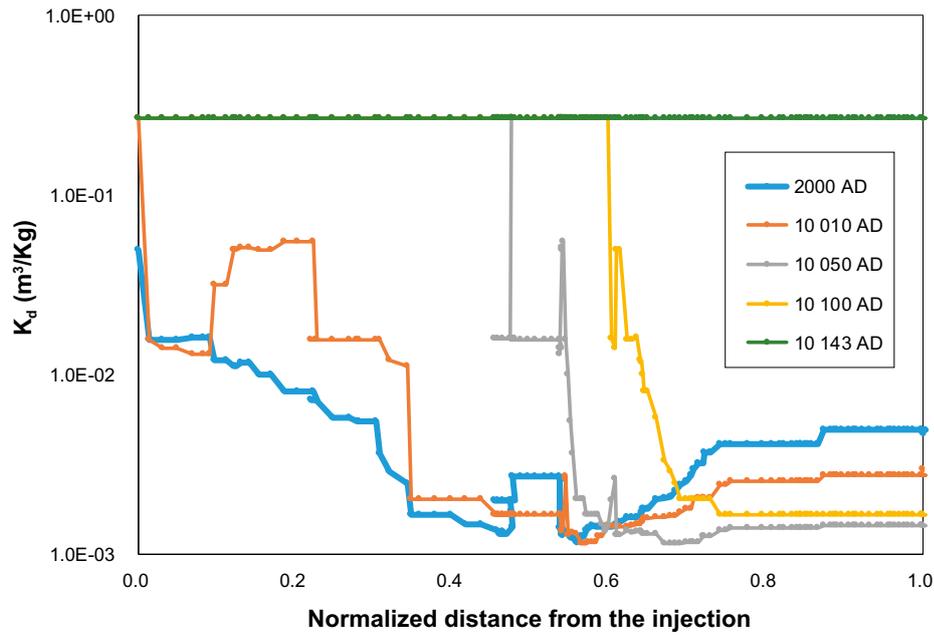
Figure 4-24. K_d values computed by iFM along the selected trajectory at different times.
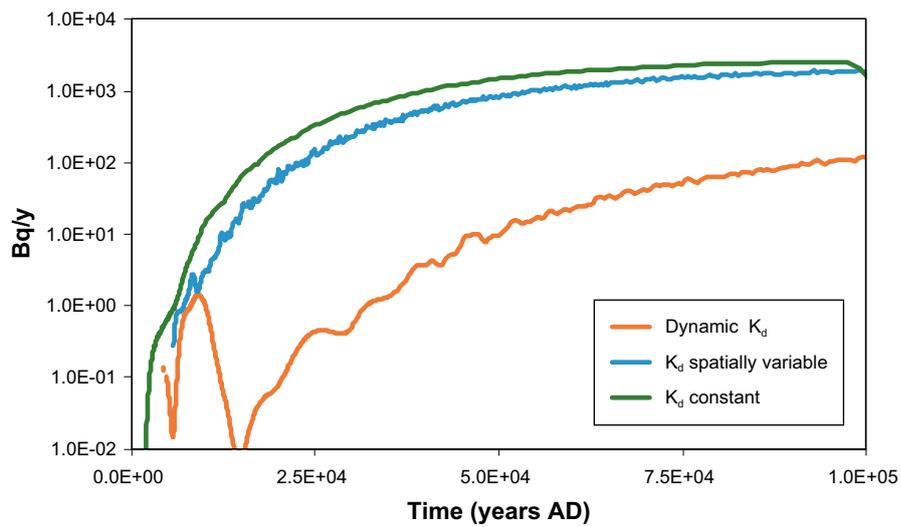
Figure 4-25. Breakthrough curves for Ni-59 computed using K_d constant (see Section 4.2), K_d spatially variable and the dynamic K_d approach.

5 Analysis of possible mechanisms of molybdenum retention

5.1 Conceptual model for molybdenum sorption

Molybdenum-93 (Mo-93, with a half-life of 4 000 years) is an activation product that will be produced whenever Mo-containing materials are exposed to neutron radiation. It has emerged as an important radionuclide in the assessments of post-closure safety for SFR and SFL (SKB 2014).

No extensive thermodynamic information for Mo is available (see for example Dellien et al. (1976), who performed a critical review on the Mo thermodynamic properties). In the present work, we have used the ThermoChimie database (see Giffaut et al. 2014, and http://www.thermochimie-tdb.com/) as a source of thermodynamic information. In ThermoChimie, thermodynamic data selection for molybdenum compounds (specifically stability constants for formation reactions) is based on data available in the literature (e.g. Aveston et al. 1964, Sasaki and Sillén 1968, O'Hare 1974).

The predominance diagram (Figure 5-1) indicates that, under reducing conditions, and if enough Molybdenum is present in the system, solid Mo(IV) oxide may be stable. It should be noticed that the thermodynamic data for $MoO_2(s)$ included in ThermoChimie, from Robie et al. (1979), corresponds to a crystalline solid which is unlikely to precipitate under repository conditions.

The most relevant molybdenum form in repository and geosphere conditions is Mo(VI) and specifically the molybdate ion, MoO_4^{2-} (SKB 2014). This is illustrated in the predominance diagram in Figure 5-1, where the blue rectangle represents the pH and Eh characteristic of groundwaters in SFL repository, taking into account the statistical distributions (25th and 75th percentiles) reported by Joyce et al. (2019) at different times.

Since molybdate is negatively charged, it is not expected to sorb strongly on the bedrock, and frequently it has been assumed to be non-sorbing in transport calculations (Crawford 2013). However, given the relatively short half-life of the principal Mo radioactive isotope (Mo-93), the activity that could potentially reach the surface is strongly dependant on possible (even weak) retention processes in the bedrock (Lidman et al. 2016). Possible minerals for molybdate sorption would primarily be those that have point of zero charge near normal pH, for example certain aluminosilicates or iron oxides (Lidman et al. 2016). This is discussed in the sections below.

It is worthwhile noting that, besides being a realistic assumption based on what discussed above, i.e. assuming that molybdate is the predominant molybdenum species, it is in addition a conservative assumption as the other metastable phases are not mobile.
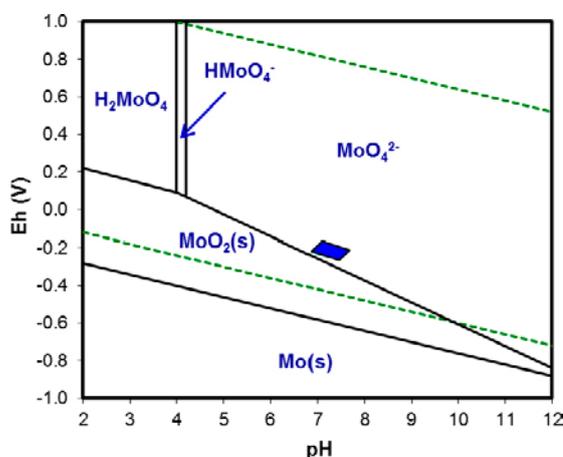
Figure 5-1. *Mo predominance diagram calculated using ThermoChimie database and with a total Molybdenum concentration of 1 × 10-10 M. The blue rhomboid represents pH-Eh values for characteristic groundwaters in SE-SFL, according to Joyce et al. (2019).*

Further, in the present work we have not taken into account the possible Mo sorption in clay materials, even if clays are expected to be present in the bedrock at the Laxemar site. On the contrary, efforts have been focused on Mo sorption on iron materials (see sections below).

5.1.2 Molybdenum sorption on goethite

Goethite may be present in the bedrock at the Laxemar site, especially in the fractures near the surface (see Figure 6-7 in Drake and Tullborg 2009).

Mo sorption on goethite has been studied by different authors; two of the most detailed and complete studies are those of Goldberg et al. (1996, 1998) and that of Xu et al. (2006).

Goldberg et al. (1996, 1998) studied Molybdenum adsorption behaviour on various materials, including crystalline and X-ray amorphous Fe oxide minerals. According to their results, sorption depends on the type of oxide studied, but maximum adsorption occurs at pH ≈5 in most cases. Above pH 5, sorption is smaller.

Xu et al. (2006) studied MoO_4^{2-} sorption on goethite; they also observed a decrease in sorption at pH values above 5. The competitive effects other oxoanions (sulfate, phosphate, and silicate) were also studied by Xu et al. (2006); phosphate exhibit a highly competitive behaviour; silicate showed a minor competition, while sulphate did not show any competition effect. Phosphate concentrations in groundwater are expected to be low, probably limited by hydroxyapatite ($Ca_5(PO_4)_3(OH)(s)$) (see Bruno et al. 2001). Thus, phosphate competition is not expected to play a key role in Mo adsorption in the bedrock at the Laxemar site.

Goldberg et al. (1996) and Xu et al. (2006) performed their experiments under slightly different conditions (see Table 5-1). A comparison of the results obtained in both studies is shown in Figure 5-2.

Table 5-1. Comparison of experimental conditions for MoO_4^{2-} sorption on goethite in Goldberg et al. (1996, 1998) and Xu et al. (2006).

MoO_4^{2-} sorption on goethite	Goldberg et al. (1996, 1998)	Xu et al. (2006)
[Mo]initial (µmol/l)	292	50
Solid/Liquid ratio (g/l)	1.25	0.3
Surface area (m²/g)	63.7	43.96
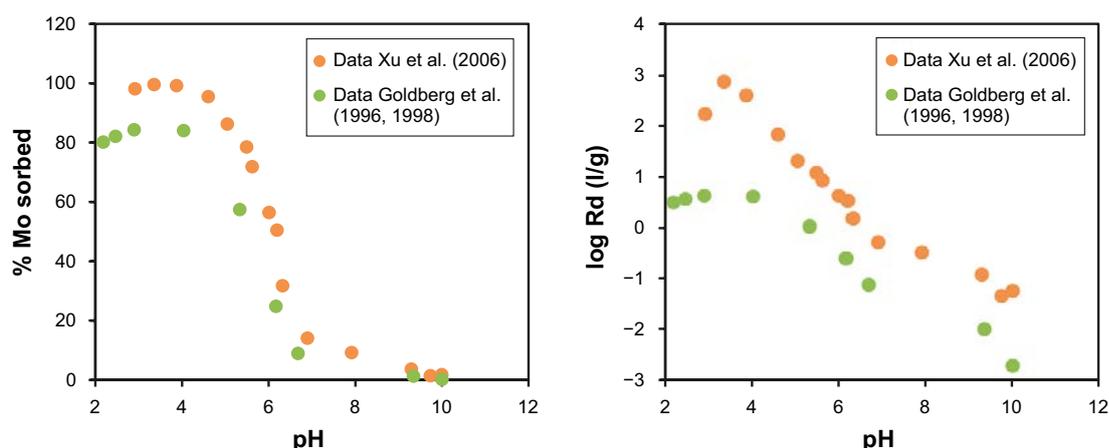
Figure 5-2. *Molybdate adsorption on goethite (left: % Mo sorbed; right: log Rd values) as a function of solution pH. Orange circles: experimental data from Xu et al. (2006). Green circles: experimental data from Goldberg et al. (1996, 1998).*

In present work, we have developed a simplified model in order to explain MoO_4^{2-} sorption on goethite, based on the assumption that Mo(VI) will sorb on Fe-OH sites. The model is based on the following hypothesis:

• The role of the electrostatic layer has not been taken into account.

• We have assumed that Mo sorbs on surface hydroxyl functional groups of goethite (Surf-OH sites), forming inner-sphere complexes (see for example Goldberg et al. 1998).

• The number of reactive surface sites for goethite has been set to 2.54×10^{-4} mol/g (this is, 5.8×10^{-6} mol/m² for a goethite solid with a surface area of 44 m²/g, in agreement with the data reported in Xu et al. 2006). This value is in agreement with the number of sites of 3.8×10^{-6} mol/m² suggested by Davis and Kent (1990) for natural materials.

• Protonation/deprotonation constants for the surface functional groups are shown in Equation 5-1 and Equation 5-2. These values are very similar to the ones recommended in Dzombak and Morel (1990). for protonation/deprotonation constants in hydrous ferric oxides.

Surf_OH + H⁺ = Surf_OH₂⁺	Log K = 7.18	Dzombak and Morel (1990)	Equation 5-1
Surf_OH = Surf_O⁻ + H⁺	Log K = −8.82	Dzombak and Morel (1990)	Equation 5-2

• The model includes two Mo inner surface complexes with goethite. We have assumed that under acidic conditions, $HMoO_4^-$ will sorb on $Fe-OH_2^+$ (Equation 5-3). Under near-neutral conditions, MoO_4^{2-} will sorb on $Fe-OH_2^+$ (Equation 5-4). The constants for those sorption processes have been fitted in present work in order to be in agreement with the experimental results from Xu et al. (2006), as seen in Figure 5-3.
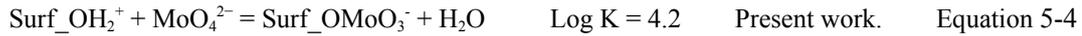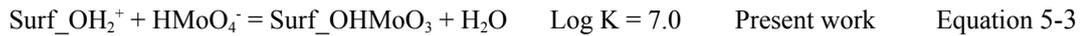
Surf_OH₂⁺ + HMoO₄⁻ = Surf_OHMoO₃ + H₂O	Log K = 7.0	Present work	Equation 5-3
Surf_OH₂⁺ + MoO₄²⁻ = Surf_OMoO₃⁻ + H₂O	Log K = 4.2	Present work.	Equation 5-4

This simplified model is able to explain the results obtained in Xu et al. (2006) for MoO_4^{2-} sorption on goethite, as shown in Figure 5-3, as long as the protonation/deprotonation constants and the number of sites described above are used.

As shown in the figure, more inaccurate results are obtained in those pH regions where sorption is nearly 100 % or nearly 0. In those zones is normally more difficult to obtain accurate measurements (due to low Mo amounts in solution or sorbed), and the experimental error is expected to be higher.
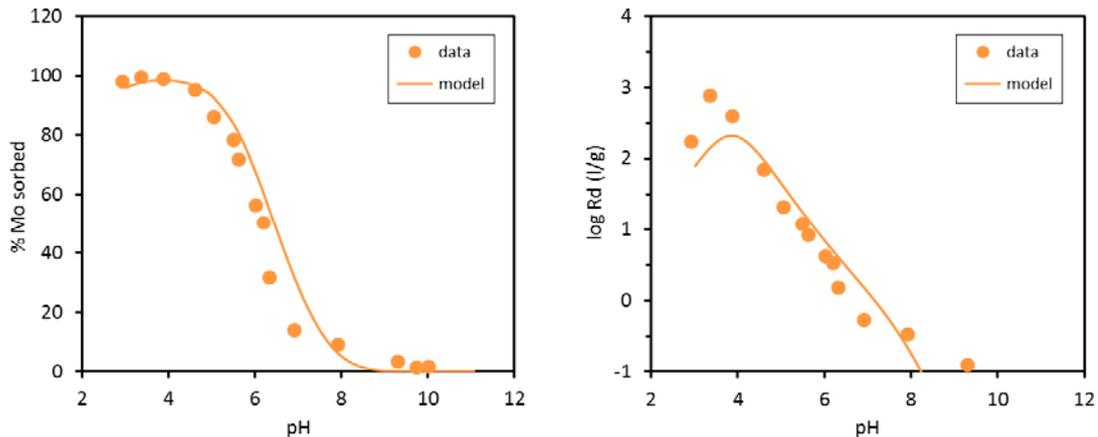
Figure 5-3. *Molybdate adsorption on goethite as a function of solution pH (left: % Mo sorbed; right: log Rd values). Orange circles: experimental data from Xu et al. (2006). Solid line: modelling of the data performed in present work (see text).*

Some complex sorption calculations available in the literature are based on Constant Capacitance Model or in the Triple Layer Model (Goldberg et al. 1998). However, those models are expected to lead to convergence problems, even in simplified batch reactions calculations (see for example Goldberg et al. 1966) and are difficult to implement in complex transport calculations. Thus, in the calculations developed in present work, the role of the electrostatic layer has not been taken into account. This means that the constants fitted in present work are optimized for its use *without* an electric double layer; including the electric layer in the calculations would lead to a worse data fit (see Figure 5-4).

5.1.3 Molybdenum sorption on pyrite

Pyrite is expected to be present in the bedrock at the Laxemar site (see Löfgren and Sidborn 2010 and Figure 6-7 in Drake and Tullborg 2009).

Molybdate (MoO_4^{2-}) sorption on pyrite has been studied by Bostick et al. (2003) and Xu et al. (2006). The conditions of Bostick et al. (2003) and Xu et al. (2006) experiments are summarized in Table 5-2.

Table 5-2. Comparison of experimental conditions for MoO_4^{2-} sorption on pyrite in Bostick et al. (2003) and Xu et al. (2006).

MoO_4^{2-} sorption on pyrite	Bostick et al. (2003)	Xu et al. (2006)
[Mo]initial (µmol/l)	0–100	0–200
Solid/Liquid ratio (g/l)	1	2
Surface area (m²/g)	41.7	0.89

The results obtained by Bostick et al. (2003) and Xu et al. (2006) show that maximum adsorption occurs at pH < 5; above pH 5, sorption is smaller. Results obtained by Bostick et al. (2003) and Xu et al. (2006) for MoO_4^{2-} sorption on pyrite as a function of pH are compared Figure 5-5.

In the present work, we have developed a simplified model in order to explain MoO_4^{2-} sorption on pyrite. The model is based on the assumption that Mo(VI) will sorb on Fe-OH sites in the surface of pyrite. The model is analogous to that developed for MoO_4^{2-} sorption on goethite; the only difference is the number of sites for each mineral used in the calculations. The number of reactive surface sites for pyrite has been set to 3.8×10^{-5} mol/g (this is, 4.3×10^{-5} mol/m² for a pyrite solid with a surface area of 0.89 m²/g, in agreement with the data reported in Xu et al. 2006).
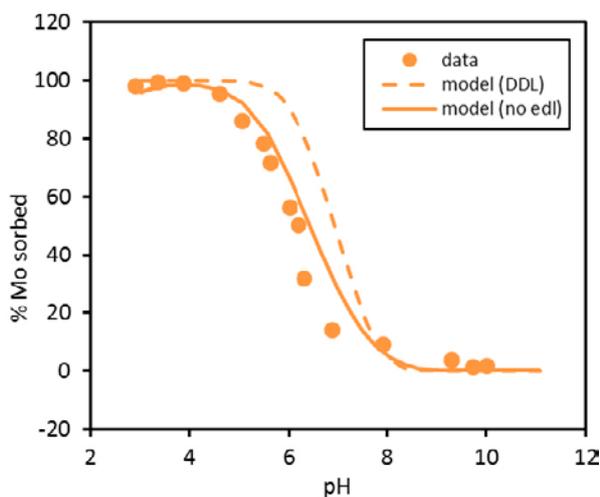
Figure 5-4. *Molybdate adsorption on goethite as a function of solution pH. Orange circles: experimental data from Xu et al. (2006). Solid line: modelling of the data performed in present work. Dashed line: modelling, including the diffuse layer.*
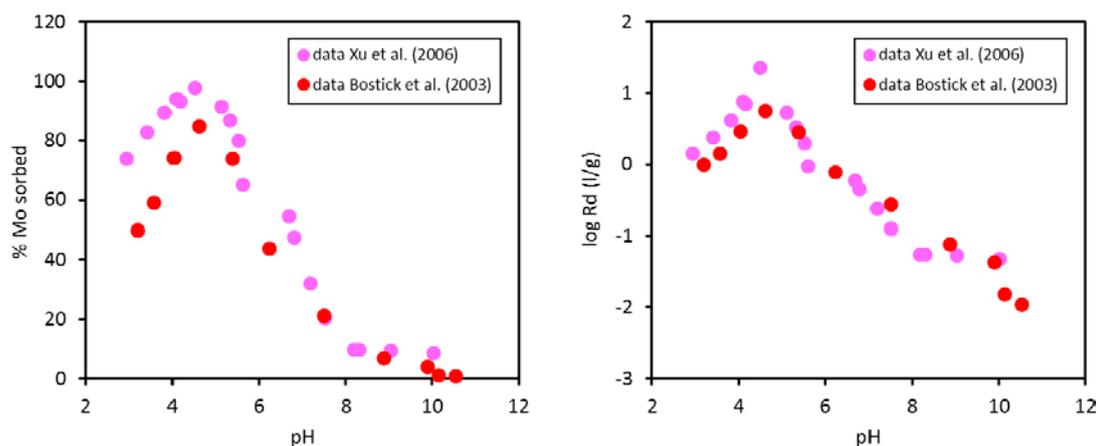
Figure 5-5. Molybdate adsorption on pyrite as a function of solution pH (left: % Mo sorbed; right: log Rd values). Pink circles: experimental data from Xu et al. (2006). Red circles: experimental data from Bostick et al. (2003).

This simplified model is able to explain the results obtained in Xu et al. (2006) for MoO_4^{2-} sorption on pyrite, as shown in Figure 5-6. As in the case of goethite, more inaccurate results are obtained in those pH regions where sorption is nearly 100 % or nearly 0, as the experimental error is expected to be higher.

Tetrathiomolybdate (MoS_4^{2-}) sorption on pyrite has also been studied by Bostick et al. (2003) and Xu et al. (2006). In both cases, tetrathiomolybdate sorption was shown to be stronger than that of molybdate.

In sulphidic water molybdate may react with sulphide to form thiomolybdates (Dahl et al. 2013). However, Mo thermodynamic data are limited; specifically, no reliable thermodynamic data for aqueous Mo-S species are available. Therefore, the formation and sorption of tetrathiomolybdates or other Mo-S aqueous species in the bedrock at the Laxemar site cannot be taken into account in the calculations, and the possible sorption of these species on pyrite cannot be modelled.

However, as shown in Xu et al. (2006) or Bostick et al. (2003), sorption of tetrathiomolybdate in pyrite is equal or higher than molybdate sorption on pyrite. Thus, neglecting the effect of tetrathiomolybdate species in present work may be regarded as a conservative approach.
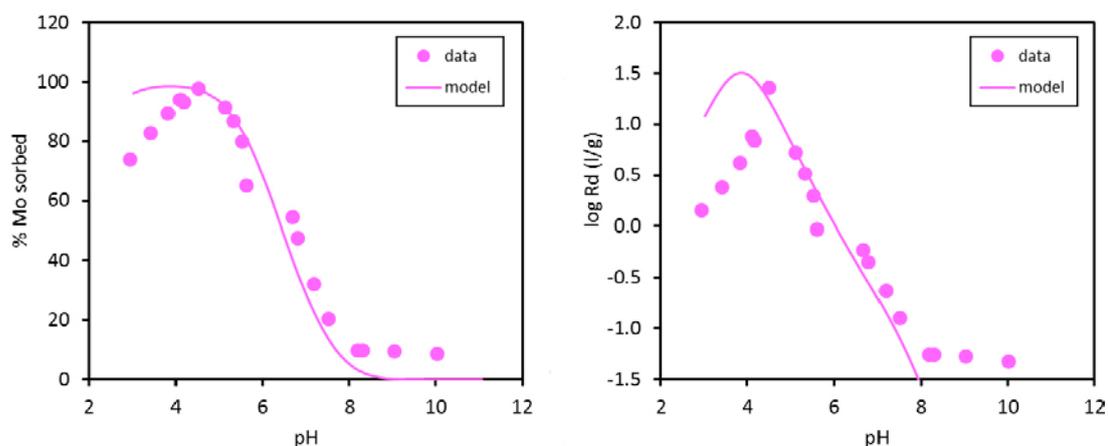

Figure 5-6. Molybdate adsorption on pyrite as a function of solution pH (left: % Mo sorbed; right: log Rd values). Pink circles: experimental data from Xu et al. (2006). Solid line: modelling of the data performed in present work.

5.1.4 Conceptual model for Mo sorption: summary

We have developed a unique simplified model in order to explain MoO_4^{2-} sorption onto both goethite and pyrite. The model is based on the assumption that Mo(VI) will sorb on the surface hydroxyl groups of those minerals; it includes protonation/deprotonation constants for hydroxyl groups and the formation of two different surface complexes with Mo(VI). The model does not take into the role of the electrostatic layer in order to avoid converge problems in transport calculations.

$Surf\_OH + H^+ = Surf\_OH_2^+$	Log K = 7.18	Equation 5-5
$Surf\_OH = Surf\_O^- + H^+$	Log K = −8.82	Equation 5-6
$Surf\_OH_2^+ + HMoO_4^- = Surf\_OHMoO_3 + H_2O$	Log K = 7.0	Equation 5-7
$Surf\_OH_2^+ + MoO_4^{2-} = Surf\_OMoO_3^- + H_2O$	Log K = 4.2	Equation 5-8

The number of reactive surface sites has been set to 2.54×10^{-4} mol/g for goethite and 3.8×10^{-5} mol/g for pyrite.

This simplified model is able to explain the results obtained in Xu et al. (2006) for MoO_4^{2-} sorption on goethite and pyrite, and indicates that sorption of MoO_4^{2-} in goethite or pyrite under groundwater conditions may be small but non-negligible. Furthermore, due to the lack of reliable thermodynamic data, the model does not include thiomolybdate formation neither sorption. Taking into account that thiomolybdate sorption on pyrite is expected to be stronger than that of MoO_4^{2-}, the model can be regarded as conservative.

5.2 Anchoring the Mo sorption model to field data from Laxemar

Figure 5-7 shows the occurrence of goethite and pyrite in two different shallow boreholes at Laxemar. From the figure and from other field evidence (Drake and Tullborg 2009) it is evident that goethite is mostly present in the very shallow and altered bedrock at Laxemar. Pyrite is instead found with high frequency at lower depths Thus, the model has been parameterised assuming that pyrite is the only available reactive mineral in the all model domain. It is worthwhile noting that, with the current version of iFM and MARFA, this simplification can be easily relaxed by using different rocktypes associated with different reactive minerals.

The density of sorption sites ($S[mol/L]$) is given by:

$$S = \frac{S_m \cdot \rho_m \cdot \omega}{\Phi}$$ Equation 5-9

where S_m is the site density relative to the mass of mineral (mass site density, from now onward [mol/kg_m], ρ_m is the mineral density [kg_m/m_m^3], Φ is the matrix porosity and ω is the mineral volume fraction m_m^3/m_b^3.
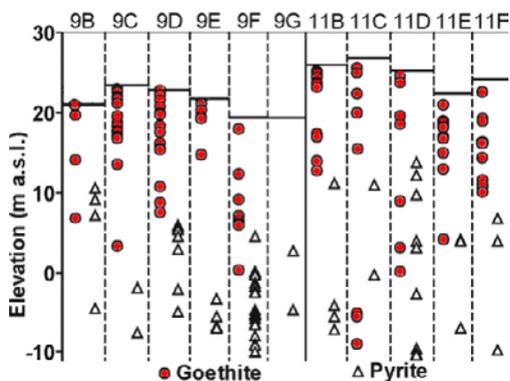
Figure 5-7. *Occurrence of goethite (circles) and pyrite (triangles) in KLX09B–G and KLX11B–F at Laxemar (taken from Drake and Tullborg 2009).*

The values of porosity and density have been set to 3×10^{-3} and 3×10^6 g/m^3, respectively; i.e. typical values for a fractured crystalline rock. The mass site density has already been introduced in Section 5.1.3 and for pyrite a value of 3.8×10^{-5} mol/g is considered. Information about plausible values of pyrite volume fraction are taken from Table A1-11 of Drake and Tullborg (2009), which provides the mineralogical composition of red-stained Ävrö granite (i.e. the dominating rocktype at Laxemar). Pyrite is found to be present in a very minor amount, with an average volume fraction (median value) lower than 0.1 % and a maximum of 0.19 %. Thus, two calculations have been carried out, one with a high value of volume fraction (i.e. the highest value provided in Drake and Tullborg (2009) – $\omega^{high} = 1.9 \times 10^{-3}$) and a second simulation with a low volume fraction ($\omega^{low} = 1.9 \times 10^{-5}$).

5.3   MARFA calculations with high number of sorption sites

The radionuclide transport calculations (MARFA SP calculations) were carried out along the ensemble of trajectories starting from BHA (Figure 4-9). The release functions for Mo-93 (4 000 y half-life) were obtained from results of Ecolego near-field calculations (Figure 5-8).

Three independent set of calculations were performed:

- *No-retention calculations* => K_d is set to zero. This is the typical assumption used in molybdenum transport models from previous safety assessment studies (e.g. Crawford 2013).

- *K_d spatially variable calculations* => spatially variables K_d values computed by iFM using background geochemistry computed at 2000 AD by Joyce et al. (2019). No temporal update of K_d values.

- *Dynamic K_d calculations* => spatially variable K_d values computed by iFM (2000 AD) and updated at 5000 AD, 20 000 AD and 60 000 AD with background geochemistry taken from Joyce et al.(2019).

The breakthrough curves for Mo-93 are shown in Figure 5-9. A "Base Case" calculation was run assuming no sorption for molybdenum; i.e. the typical assumption used in previous safety assessment studies. It can be noticed that by defining initially heterogeneous conditions (i.e. K_d values computed at 2000 AD but no update in time) the retention capacity of the system is significantly increased with the peak value that is decreased to less than one third of the value obtained with the no-retention calculation. When K_d values are updated in time no significant changes are observed. This along with other implications of these results is discussed in detailed in the next sub-section.
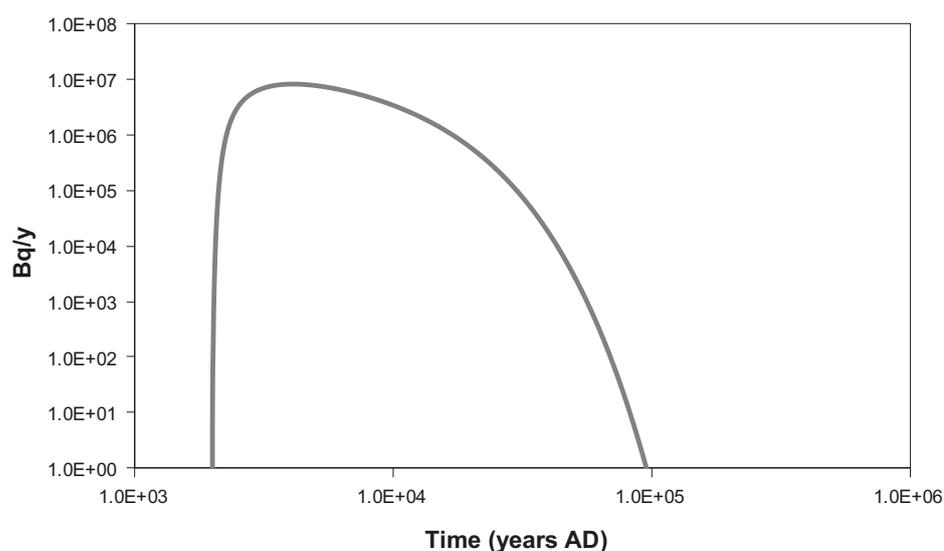
Figure 5-8. Release function for molybdenum at BHA as computed by Ecolego near-field calculations.
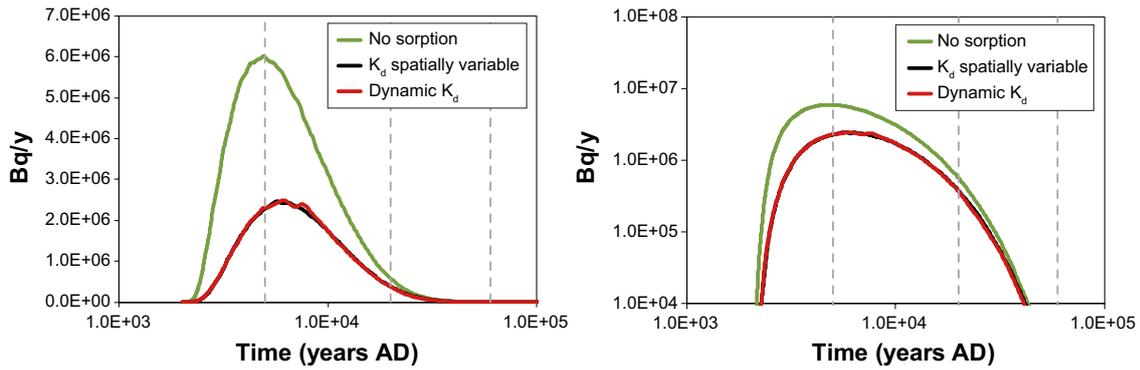
Figure 5-9. *Breakthrough curves of Mo-93 (left: semilog scale; right: log-log scale) computed using $K_d = 0$, K_d spatially variable and the dynamic K_d approach. Vertical dashed lines indicate the time of the update of K_d values. The iFM calculations are carried out with the high value of pyrite volume fraction.*

5.3.1 Inconsistency of the calculation

The temporal evolution of K_d values along a selected trajectory is shown in Figure 5-10. If compared with the nickel K_d values discussed in Chapter 4, the values of molybdenum partitioning coefficients are about one or half order of magnitude lower, which overall means still a considerable retention. The modest changes observed at the different updating temporal windows explain the apparent insensitivity observed in the breakthrough curves when the K_d values are updated in time (Figure 5-9).

However, the dependence between K_d values and pH (Figure 5-11) shows some inconsistency. In fact, according to the conceptual model of Mo sorption onto pyrite (Section 5.1.3), a negative correlation should be expected (i.e. higher K_d values with more acidic conditions). The results of Figure 5-11 are explained by the very high density of sites of this calculation. In fact, the value of pH represented in the figure is the input value provided to Phreeqc (i.e. the pH value computed by ConnectFlow). However, after equilibration, this value is changed by protonation reactions and conditions tend to near-alkaline values (pH~8). These results violate the basic hypothesis of the dynamic K_d approach that assumes that sorption reactions do not affect major chemistry. The purpose of this set of calculations is precisely to illustrate a non-realistic situation where the sorption model has a strong control on background geochemistry. In the next section we will show a more realistic set of models where a lower amount of sorption, based on a more realistic amount of pyrite, sites does not affect the evolution of background geochemistry.
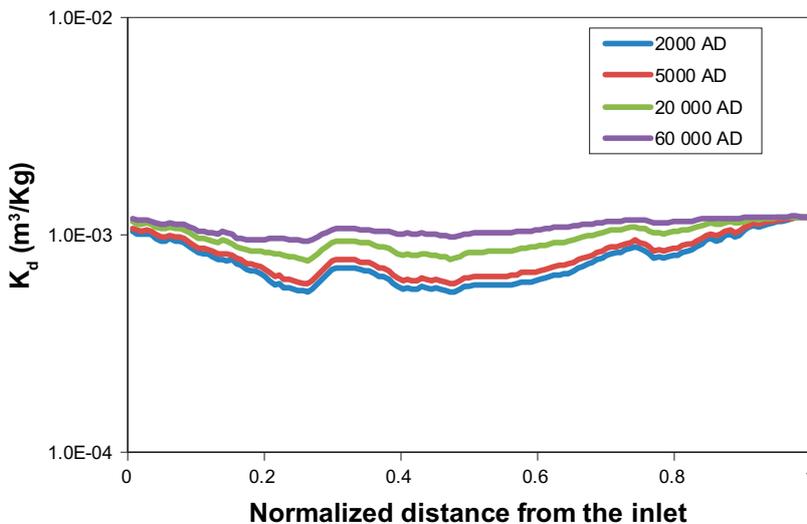
Figure 5-10. *K_d values of Mo-93 computed by iFM along a single trajectory at different times. The iFM calculations are carried out with the high value of pyrite volume fraction.*
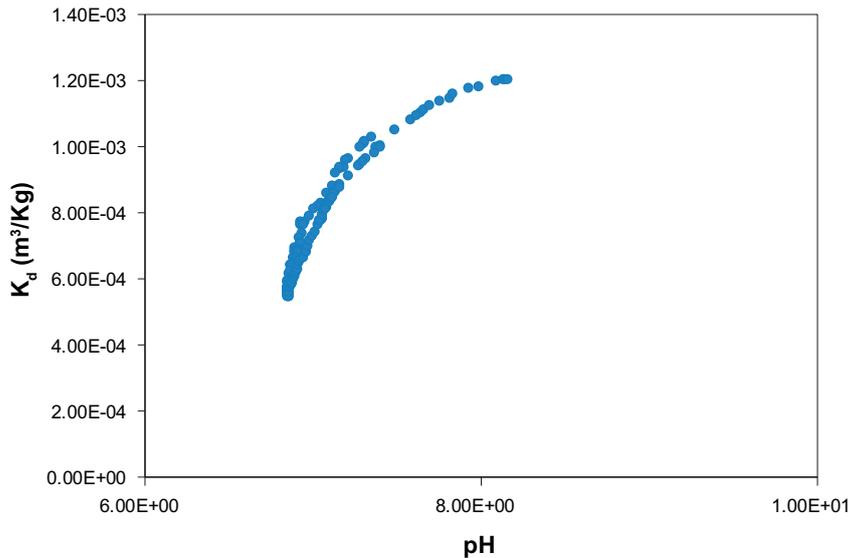
Figure 5-11. K_d *values versus pH, at time 2000 AD. Each dot represents a single trajectory segment of the selected trajectory. The iFM calculations are carried out with the high value of pyrite volume fraction.*

5.4 MARFA calculations with low number of sorption sites

The breakthrough curves of Mo-93 are shown in Figure 5-12. As expected, when a lower density of sites is considered, the retention of molybdenum decreases considerably. However, even when using a low abundance of pyrite (the value used in these calculations should be considered as a lower bound for the Laxemar site) a decrease of about 16 % of the peak value is observed. As in the previous case, results seem to be insensitive to the update of K_d values. This is related to the modest change in K_d values observed at the different updating time windows (Figure 5-13), which is in turn related to the strong control of pH on Mo retention. In the ConnectFlow reactive transport model in fact pH is strongly buffered by calcite and thus small changes in retention properties are observed.

The scatter plot showing the relationship between pH and K_d at 2000 AD and for a single trajectory is shown in Figure 5-14. The negative correlation between the two parameters (i.e. decreasing K_d with increasing pH) is now consistent with the underlying conceptual model. This indicates that, with the low amount of sorption sites, sorption processes do not have any influence of background geochemical conditions, meaning that the basic premise of the dynamic K_d approach holds true.
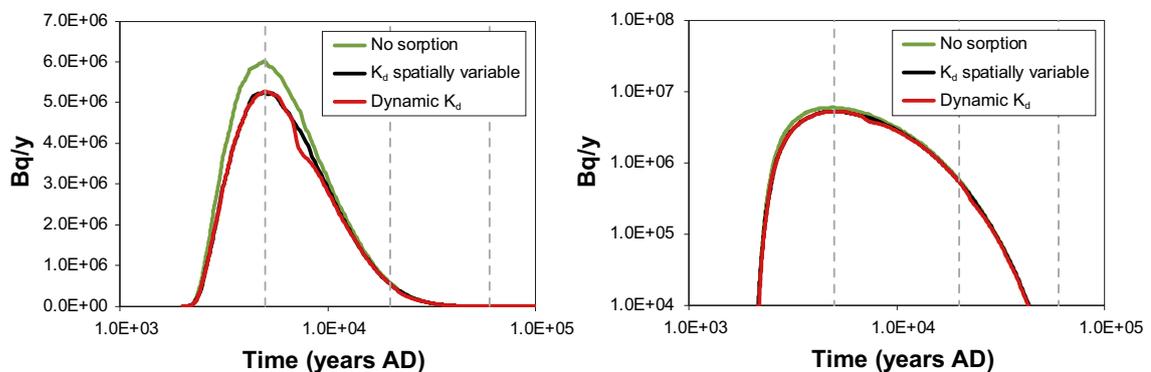
Figure 5-12. *Breakthrough curves of Mo-93 (left: semilog scale; right: log-log scale) computed using* $K_d = 0$, K_d *spatially variable and the dynamic* K_d *approach. Vertical dashed lines indicate the time of the update of* K_d *values. The iFM calculations are carried out with the low value of pyrite volume fraction.*
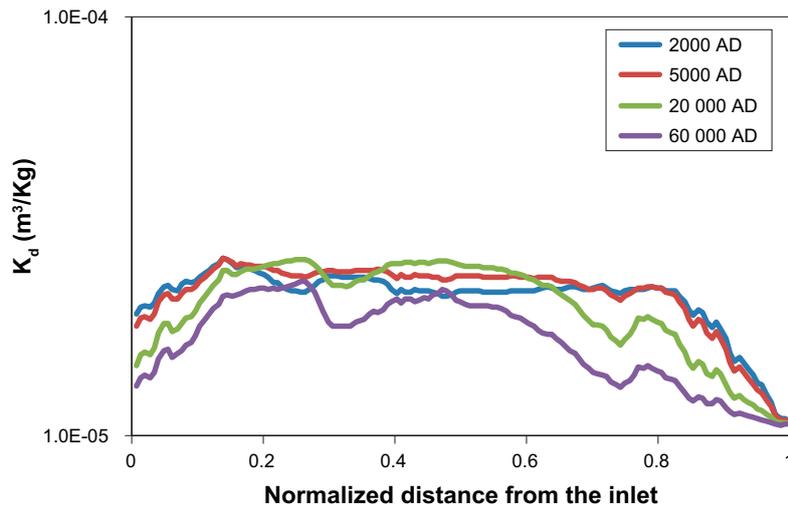
Figure 5-13. *K_d values of Mo-93 computed by iFM along a single trajectory at different times. The iFM calculations are carried out with the low value of pyrite volume fraction.*
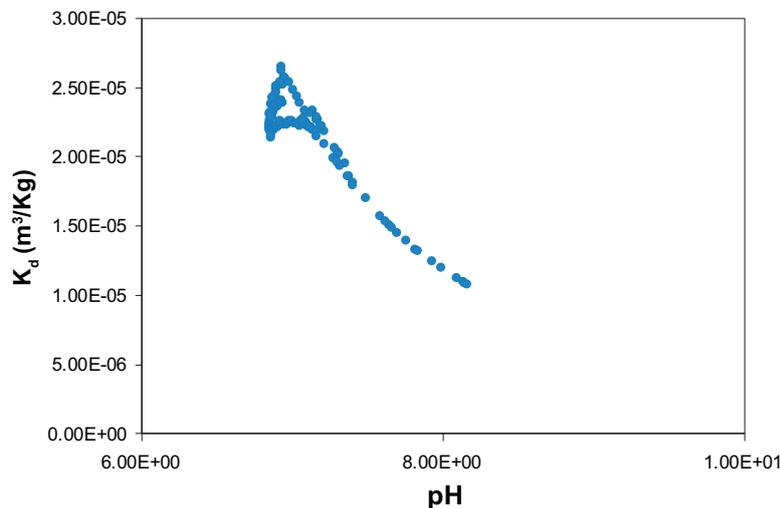

Figure 5-14. *K_d values versus pH, at time 2000 AD. Each dot represents a single trajectory segment of the selected trajectory. The iFM calculations are carried out with the low value of pyrite volume fraction.*

Overall, the results presented in Chapter 5 show that in the bedrock at Laxemar molybdenum is retained in the matrix mostly by the available pyrite grains. The calculations presented in this section point out that even considering a very low amount of pyrite a decrease of 16 % of the peak concentration is obtained. Goethite, mostly present in the shallow bedrock, along with more acidic conditions that are likely to be attained in the very shallow part of the bedrock at Laxemar are additional buffering mechanisms that should be carefully assessed in future safety assessment studies.

6 Summary and conclusions

We have applied the dynamic K_d approach (Trinchero et al. 2016) in the context of the SE-SFL safety evaluation project. The objective of the modelling work is to demonstrate that the approach and related software (iFM and MARFA) are mature and that their use in the context of safety assessment studies for nuclear waste repositories can provide significant advantages in terms of reduction of unnecessary conservatism and improvement of model realism.

The numerical analysis has focused on nickel and molybdenum transport and retention.

Nickel has been shown to be particularly sensitive to the progressive decrease in salinity, which is expected in Laxemar due to the progressive increasing signature of infiltration processes under the assumption of constant temperature climate conditions. Over a temperate period, nickel retention can increase significantly due to the decreasing of competition for sorption sites and the lower aqueous complexation. This increase in retention, which is not captured by "standard" K_d-constant approaches, provides an important additional buffer against the release of repository-derived nickel to the biosphere. This buffering effect is even more pronounced for isotope nickel-63 due to its short half-life.

Another radionuclide that has been assessed in this study is molybdenum, which in previous safety assessment studies was treated as non-sorbing radionuclide. Data from the literature have been used to derive a new surface complexation model on goethite and pyrite. Available mineralogical information for pyrite at Laxemar has been used to parameterise the model. The results of the dynamic K_d calculations show that molybdenum can be weakly sorbed onto the available reactive minerals and that this retention processes will reduce the peak concentration by around 20 %. This reduction is obtained using a conservative estimate of the available amount of sorption sites.

Overall, the project has pointed out the feasibility of applying dynamic K_d calculations in the context of complex safety analyses of nuclear waste repositories. Given the long time frame of these analyses, with the dynamic K_d-approach one is able to capture the influence of changes in geochemical conditions that are otherwise neglected in "standard" K_d-constant calculations. The results of the dynamic K_d simulations are more realistic and reduce the unnecessary conservatism of K_d-constant calculations.

References

SKB's (Svensk Kärnbränslehantering AB) publications can be found at www.skb.com/publications.

Auqué L F, Gimeno M J, Acero P, Gómez J B, 2013. Composition of groundwater for SFR and its extension, during different climatic cases, SR-PSU. SKB R-13-16, Svensk Kärnbränslehantering AB.

Aveston J, Anacker E W, Johnson J S, 1964. Hydrolyses of molybdenum(VI). Ultracentrifugation, acidity measurements, and raman spectra of polymolybdates. Inorganic Chemistry 3, 735–746.

Bostick B C, Fendorf S, Helz G R, 2003. Differential adsorption of molybdate and tetrathiomolybdate on pyrite (FeS_2). Environmental Science & Technology 37, 285–291.

Bradbury M, Baeyens B, 2009. Sorption modelling on illite Part I: Titration measurements and the sorption of Ni, Co, Eu and Sn. Geochimica et Cosmochimica Acta 73, 990–1003.

Bruno J, Duro L, Grivé M, 2001. The applicability and limitations of the geochemical models and tools used in simulating radionuclide behaviour in natural waters. Lessons learned from the Blind Predictive Modelling exercises performed in conjunction with Natural Analogue studies. SKB TR-01-20, Svensk Kärnbränslehantering AB.

Crawford J, 2013. Quantification of rock matrix K_d data and uncertainties for SR-PSU. SKB R-13-38, Svensk Kärnbränslehantering AB.

Dahl T W, Chappaz A, Fitts J P, Lyons T W, 2013. Molybdenum reduction in a sulfidic lake: Evidence from X-ray absorption fine-structure spectroscopy and implications for the Mo paleoproxy. Geochimica et Cosmochimica Acta 103, 213–231.

Davis J A, Kent D B, 1990. Surface complexation modeling in aqueous geochemistry. In Hochella M F, White A F (eds). Mineral-water interface geochemistry. Washington, DC: Mineralogical Society of America. (Reviews in mineralogy 23), 177–260.

Dellien I, Hall F M, Hepler L G, 1976. Chromium, molybdenum, and tungsten: thermodynamic properties, chemical equilibriums, and standard potentials. Chemical Reviews 76, 283–310.

Drake H, Tullborg E-L, 2009. Fracture mineralogy Laxemar. Site descriptive modelling SDM-Site Laxemar. SKB R-08-99, Svensk Kärnbränslehantering AB.

Duro L, Grivé M, Cera E, Domènech C, Bruno J, 2006. Update of a thermodynamic database for radionuclides to assist solubility limits calculation for performance assessment. SKB TR-06-17, Svensk Kärnbränslehantering AB.

Dzombak D A, Morel F M M, 1990. Surface complexation modeling: hydrous ferric oxide. New York: Wiley.

Giffaut E, Grivé M, Blanc P, Vieillard P, Colàs E, Gailhanou H, Gaboreau S, Marty N, Madé B, Duro L, 2014. Andra thermodynamic database for performance assessment: ThermoChimie. Applied Geochemistry 49, 225–236.

Gimeno M, Auqué L F, Gómez J B, Salas J, Molinero J, 2010. Hydrogeochemical evolution of the Laxemar site. SKB R-10-60, Svensk Kärnbränslehantering AB.

Goldberg S, Forster H S, Godfrey C L, 1996. Molybdenum adsorption on oxides, clay minerals, and soils. Soil Science Society of America Journal 60, 425–432.

Goldberg S, Su C, Forster H S, 1998. Sorption of molybdenum on oxides, clay minerals, and soils. In Jenne E A (ed). Adsorption of metals by geomedia: variables, mechanisms, and model applications. San Diego, CA: Academic Press, 401–426.

Joyce S, Appleyard P, Hartley L, Tsitsopoulos V, Woollard H, Marsic N, Sidborn M, Crawford J, 2019. Groundwater flow and reactive transport modelling of temperate conditions. Report for the safety evaluation SE-SFL. SKB R-19-02, Svensk Kärnbränslehantering AB.

Lidman F, Källström K, Kautsky U, 2016. Mo-93 from the grave to the cradle. Report from a workshop on molybdenum in radioactive waste and in the environment. SKB P-16-22, Svensk Kärnbränslehantering AB.

Löfgren M, Sidborn M, 2010. Statistical analysis of results from the quantitative mapping of fracture minerals in Laxemar. Site descriptive modelling – complementary studies. SKB R-09-31, Svensk Kärnbränslehantering AB.

O'Hare P A G, 1974. Thermochemistry of molybdates III. Standard enthalpy of formation of barium molybdate, and the standard entropy and standard Gibbs energy of formation of the aqueous molybdate ion. The Journal of Chemical Thermodynamics 6, 425–434.

Painter S, Mancillas J, 2013. MARFA user's manual: Migration analysis of radionuclides in the far field. Posiva Working Report 2013-01, Posiva Oy, Finland.

Robie R A, Hemingway B S, Fisher J R, 1979. Thermodynamic properties of minerals and related substances at 298.15 K and 1 bar (10^5 pascals) pressure and at higher temperatures. U.S. Geological Survey Bulletin 1452.

Salas J, Gimeno M J, Auqué L, Molinero J, Gómez J, Juárez I, 2010. SR-Site – hydrogeochemical evolution of the Forsmark site. SKB TR-10-58, Svensk Kärnbränslehantering AB.

Sasaki Y, Sillén I G, 1968. Equilibrium studies of polyanions. 16. Equilibria of molybdates in 3M $Na(ClO_4)$ medium at 25 °C. Arkiv för kemi 29, 253–277.

SKB, 2014. Data report for the safety assessment SR-PSU. SKB TR-14-10, Svensk Kärnbränsle-hantering AB.

Tang D, Frind E, Sudicky E A, 1981. Contaminant transport in fractured porous media: Analytical solution for a single fracture. Water Resources Research 17, 555–564.

Trinchero P, Molinero J, Román-Ross G, Berglund S, Selroos J-O, 2014. FASTREACT – An efficient numerical framework for the solution of reactive transport problems. Applied Geochemistry 49, 159–167.

Trinchero P, Painter S, Ebrahimi H, Koskinen L, Molinero J, Selroos J-O, 2016. Modelling radionuclide transport in fractured media with a dynamic update of K_d values. Computers & Geosciences 86, 55–63.

Xu N, Christodoulatos C, Braida W, 2006. Adsorption of molybdate and tetrathiomolybdate onto pyrite and goethite: effect of pH and competitive anions. Chemosphere 62, 1726–1735.

iFM SPC technical documentation

A1 Overview

iFM SPC is distinct from the previous versions regarding the following concepts:

- **The iFM input:** In iFM-SPC the trajectory and chemistry input files are derived from ConnectFlow simulation output results.

- **Binning method**: The K_d/K_a binning is conditioned upon **rock types,** which means that different rocktypes can be properly handled by iFM.

A2 Installation

iFM SPC runs on any recent 64-bit Windows computer. It can be installed on Windows by double clicking the provided setup package. During the setup procedures the location where to install iFM can be selected. All the code is written with multi-platform compatibility in mind, which means that the same code with small modifications (compilation of IPhreeqc library for Linux and update of the start scripts) will also run on Linux.

A3 iFM Algorithm

When iFM starts, it creates a log file (the location of this file is specified in the input file). It then

1. Creates a Phreeqc problem linked to an IPhreeqc DLL object.

2. Reads a **ConnectFlow PTV** file that contains information about all the particles and their positions. An overview of the PTV input file is shown at the end of this section.

3. Reads a number of **ConnectFlow VAL** files which contain the correspondent chemistry for each **time** and for all **particle positions**. The ConnectFlow VAL files are associated with their corresponding times by user. For now, there is no field in the VAL file that records the time/timestep that the data relates to (please, refer to the keyword "*timeList*" in the input configuration file for more details.)

4. Converts the chemistry file in a suitable format for phreeqc.

5. Creates a Phreeqc DLL object to be used for batch calculations.

6. Using all the particle positions read and their chemistry, a number of batch calculations is sent to the Phreeqc DLL.

7. After the batch calculations, the K_d values are evaluated using user-defined expressions defined in the input configuration file.

8. The K_d values are then written to output HDF5 files.

9. The K_d values are then binned based on rock types and additionally outputted to HDF5.

10. Finally the results are written in format suitable for Marfa (i.e. *kdbin.dat* and *kdhistory.dat*). Geochemical states, including pairs of K_d/K_a values, are calculated. For more details about the formats of the Marfa input files, see the Marfa documentation.

The schematic algorithm for iFM SPC is shown in Figure A-1.
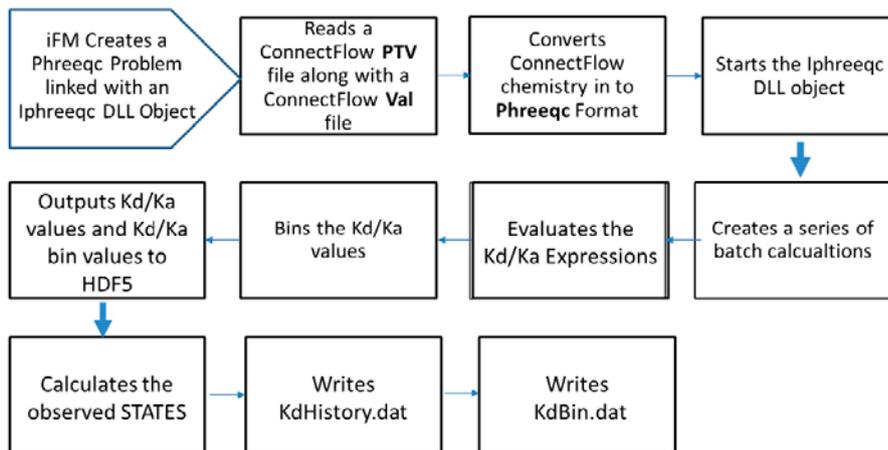
Figure A-1. *iFM SPC algorithm.*

ConnectFlow PTV format

The ConnectFlow PTV file contains the pathways used in the MARFA calculation. The format of the file is shown in Figure A-2.

```
1.  <PACKAGE> <VERSION NUMBER>
2.  <PARTICLES> <REALISATIONS> <TIMESTEPS>
3.  PART <PART NO> <REALISATION NO> <START TIME> <FLAG=0 if reaches boundary, 1 if not>
4.  <INIT X0 Y0 Z0> <FINAL XN YN ZN> <INIT VEL UX UY UZ> <TOT TIME> <TOT LENGTH>
    <F-QUOTIENT>
5.  STEPS <NO OF STEPS> this line and the following are optional
6.  <TIME> <POSITION X Y Z> <HYDRAULIC APERTURE> <TRANSPORT APERTURE> <STEP TIME>
    <F-QUOTIENT> <FLOW POTENTIAL> <ROCK NUMBER> <FRACTURE NUMBER> <FRACTURE SET>
    <MACRO FRACTURE NUMBER> <CPM/DFN ID=2> <FRACTURE NAME>
```
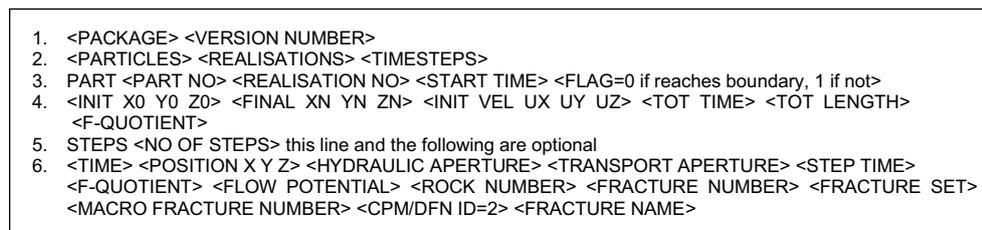
Figure A-2. *ConnectFlow PTV Format.*

ConnectFlow VAL format:

The ConnectFlow chemistry VAL files contains chemistry data for the PTV file described in Figure A-3. It has the following format:

```
1.  Header line containing the space separated list of column names.
2.  One line per point with the corresponding values for each column for that point.
    The 1st column is always the point number.
3.  The next 3 columns are always the X, Y, Z coordinates of the point.
4.  The remaining columns are the associated values for that point. In this case they are the mass
    fraction of each component (in kg per kg of solution), the charge balance (E), pH and pe.
```

Figure A-3. *ConnectFlow VAL format.*

A4   Architecture

iFM is a program written in Python 3 (http://Python.org/). It makes use of the following Python libraries:

- numpy (http://www.numpy.org/)
- h5py (http://www.h5py.org/)
- PySide (http://qt-project.org/wiki/PySide)

Included with the iFM application comes version 3.1.0–8264 of the (32-bit) IPhreeqc DLL. The HDF5 output files can be opened and viewed with HDFView (http://www.hdfgroup.org/downloads/index.html#hdfview).

Main Classes

iFM: The main class that controls iFM is called iFM which does the following:

• Sets up and initializes an iFM problem.

• Reads ConnectFlow inputs (VAL files) and converts them into phreeqc format.

• Runs a sample iFM problem with Connect Flow input data.

iFMProblemSetup: contains all the details of an iFM problem and takes care of the following tasks:

• Processes the configuration file.

• Runs the Phreeqc simulation for the reference batch.

• Post-processes the K_d/K_a and generate the Marfa input files.

The iFMProblemSetup class calls many other classes such as BatchMaker class and the Output class. The **BatchMaker** class initializes the actual chemistry for each streamline. Each BatchMaker object will control one PhreeqC DLL instance through **PhreeqCProblem**. All PhreeqC specific code is handled by this class. Writing to output files in HDF5 format, and in text format for debugging purposes, is handled by the **Output** class.

A5   Running iFM

The easiest way to run iFM is using the graphical user interface from the Windows Start Menu. This will allow you to choose the path to your input file. In the example this file is called "*inputExample.py*" and it is located in the source code directory Example folder. The input file contains all the configuration settings that are required to run iFM. For a detailed explanation of the input file structure. In case the user wants to run iFM from the command line using the Windows batch file (located in the installation folder of iFM):

> iFM.bat inputExample.py

A6   Input File Explanation

Introduction

The input file for iFM is formatted as a Python file that contains a dictionary. To explain in a clear and concise fashion the different input files of iFM and the meaning of each input variable, a simple application example has been set up and solved.

Dictionaries

The input configuration is stored in a python dictionary called **simulationConfig**. A dictionary starts with '{' and ends with '}'. It can contain several keys, and each has a value. In the IFM configuration, many of the values are dictionaries themselves. Comments start with at '#' symbol.

SimulationConfig Structure

The **simulationConfig** dictionary contains information about the input, output, log file locations, retention model, rocktypes, etc. Below we will take a look at each category and explain them in a brief manner.

The **simulationConfig** dictionary contains information about the Connect Flow input:

• **ConnectFlowInputPath**: the path to the directory containing ConnectFlow input to be used by iFM. The input provided to iFM by ConnectFlow includes a PTV path file and a number of time-related chemistry VAL files for the latter Path file with *.val extension.

• **ptvInputFile**: the name of the input file to be used by Connect Flow.

```
"ConnectFlowInputPath" : "C:/Users/hedieh/Desktop/example/ConnectFlowOutput",
"ptvInputFile" : "ptvInputFile",
```

- **timeList**: Under the keyword *timeList*, the user can associate each *.val* file with its associated time. The times are defined as a string on left side while chemistry file names are defined as string on the right side. Please note that the chemistry files have extension of *.val. When entering the file names the user should ignore the extension and only enter the file names as string.

```
"timeList" : {
                "1000" : "valInputFile1" ,
                "2000" : "valInputFile2",
             },
```

Retention Model:

Here the user can define the type of retention model to be applied. The user can choose between "ES", "MD" and "LD".

```
"retentionModel" : "LD",
```

"ES": stands for Equilibrium Sorption.

"MD": stands for Unlimited Matrix Diffusion.

"LD": stands for Limited Matrix Diffusion.

Rock Types:

Here the user can specify a string ID to be assigned to each rock type number.

```
"rockTypes" : {
                &1:   "RT1" ,
                &2:   "RT2" ,
                &3:   "RT3" ,
              },
```

This string assigned to each Rock Type number is later used under the keyword "chemInfo"/"-phreeqcContent"/"reactInWater" for defining reaction water associated to each rock type during batch calculation. The user will receive an error if there are inconsistencies between *rockTypes.dat* and "reactInWater" dictionaries. The "chemInfo" dictionary will be explained in the coming section.

Connect Flow to Phreeqc Conversion Dictionary:

Under the keyword "CFtoPhreeqc_ConversionDict", a conversion dictionary is defined. The user can optionally add/remove entries to/from this dictionary. It is important that this dictionary contains all the species in the chemistry VAL files and their corresponding phreeqc equivalents.

```
"CFtoPhreeqc_ConversionDict" : {
                                  "Al" : "Al",
                                  "pE": "pE",
                                  "Fe": "Fe",
                                  "H" : "H",
                                  "O": "O",
                                  "E": "E",
                                  "pH": "pH",
                                  "Br": "Br",
                                  "C": "C",
                                  "Ca": "Ca",
                                  "Cl": "Cl",
                                  "F": "F",
                                  "K": "K",
                                  "Li": "Li",
                                  "Mg": "Mg",
                                  "Na": "Na",
                                  "S": "S",
                                  "Si": "Si",
                                  "Sr":"Sr" ,
                                  "Mn":"Mn" ,
                                },
```

The values on the left represent chemistry symbols for ConnectFlow while the ones on the right characterize chemistry symbols of phreeqc. The conversion dictionary should contain all the chemistry symbols existing in the VAL files. If the dictionary is missing an entry, iFM will stop with the following error:

```
ConnectFlow Chemistry Symbol missing from Conversion Dictionary!
Please modify and correct the Conversion Dictionary!
```

chemInfo:

The chemInfo contains information about the geochemistry of the problem including the phreeqc input files and the radionuclide expression. Below we will explain the main parameters of this chemical dictionary. Please note that actual phreeqc input details are stored in text files located in the same folder as the configuration file.

```
"chemInfo" :
        {"phreeqcDatabase" : "base_dades_fastreact.dat",
         "phreeqcDatabaseAdditions" : "extraDBLines",
         "chemDefinitions" : {"domainChem1" : {"reactionsSolutions" : "reactInWater"}},
         "phreeqcContent" : {"extraDBLines" : "databaseAdditions.dat",
                             "radionuclidesWater":"solutionRadioNucl.dat",
                             "reactInWater":{"RT1" : "reactInWater_RT1.dat",
                                             "RT2": "reactInWater_RT2.dat",
                                             "RT3":"reactInWater_RT3.dat", }},
         "selectedOutput" :  {
                "-activities":[],
                "-equilibrium_phases":["Calcite"],
                "-saturation_indices":["Calcite"],
                "-gases":[],
                "-kinetic_reactants":[],
                "-solid_solutions":[],
                "-reset" : "true",
                "-high_precision" : "false",
                "-simulation" : "false",
                "-state" : "false",
                "-solution" : "true",
                "-time" : "true",
                "-step" : "true",
                "-ph" : "true",
                "-pe" : "true",
                "-reaction" : "false",
                "-temperature" : "false",
                "-alkalinity" : "false",
                "-ionic_strength" : "false",
                "-water" : "true",
                "-charge_balance" : "false",
                "-percent_error" : "false"},
```

phreeqcDatabase: Phreeqc database to be used by phreeqc dll.

phreeqcDatabaseAdditions: File containing the database user-modified addition lines to the phreeqc database.

PhreeqcContent: contains input files for phreeqc.

selectedOutput: Here the user can choose what to output from phreeqc. The fields under this key should comply with the phreeqc syntax.

radionuclidesWater: radionuclides to be added to the initial chemistry.

reactInWater: reactions to be added to the initial chemistry.

The second part of the chemical dictionary contains information about the radionuclide.

radioNuclInfo:

```
"radioNuclInfo" :
            {"chemDefinitions" : {"CesiumAndCalciumInfoAndKds" :
                                                {"nuclideSolution" : "radionuclidesWater",
                                                 "Kd"  : "Expressions1",
                                                 "Ka"  : "Expressions1"}},

            "Expressions" :
                        {"Expressions1" :
                                        {"exprSpecies" : {"[90Sr]":   {"outputQualifier": "totals"},
                                                          "[90Sr]X2": {"outputQualifier": "molalities"},
                                                          "[137Cs]": {"outputQualifier": "totals"},
                                                          "[137Cs]X": {"outputQualifier": "molalities"},
                                                          "[137Cs]Xa": {"outputQualifier": "molalities"},
                                                          "[137Cs]Xb": {"outputQualifier": "molalities"},
                                                         },
                                        "expressions": {
                                                        "kd":{"[90Sr]"  :  "'[90Sr]X2'/'[90Sr]'* porosity / bulkDensity",
                                                              "[137Cs]"  :  "'[137Cs]X'/'[137Cs]'* porosity / bulkDensity",},
                                                        "ka":{"[90Sr]"  :  " 0.0 ",
                                                              "[137Cs]"  :  " 0.0 ",},
                                                             },
                                        "variables" :
                                                    {"porosity" : 0.2,
                                                     "bulkDensity" : 2700.0,
                                                     "molarWeightCs" : 132.9,
                                                     "molarWeightSr" : 87.62}
                                        }
                        }
},
```

Expressions: Under this keyword, the expressions for each K_d and K_a is defined.

Variables: Here the variables used in the expressions such as porosity and bulk density are defined by user.

nuclideSolution: here the user should refer to radionuclides water defined under the "phreeqcContent".

exprSpecies: To be able to calculate the K_d values using the Phreeqc output, all the species used in the expression need to have an output qualifier defined:

Marfa Output:

iFM calculates the K_d/K_a values used by Marfa at each particle position.

```
"MarfaOutput" : {"kd" : {"[90Sr]"  : {"numberOfBins" : 1000,  "priority":1},
                         "[137Cs]" : {"numberOfBins" : 1000, "priority":2},  },
                 "ka" : {"[90Sr]"  : {"numberOfBins" : 1000, "priority":1},
                         "[137Cs]" : {"numberOfBins" : 1000, "priority":2},  },
                 "outputFiles"     : {"kdbins"    : "kdbins.dat",
                                      "kdhistory" : "kdhistory.dat"}
                }
```

Under the keyword "kd" or "ka" the user can define as many K_d/K_a expressions as required. For each K_d/K_a defined the user will need to define the following parameters.

- **Number of bins:** Number of bins to be used for binning.

- **Priority:** The priority to be used when creating STATE strings. Either of the K_d and K_a is assigned a priority value. The priority defines the order of the K_d in the state string. Below the order of the state string is defined.

    S_Kd$_1$_Kd$_2$……..Kd$_N$_Ka$_1$_Ka$_2$……Ka$_N$_RT_m

Each state starts with "S" followed by K_d values grouped in order of priority and then followed by K_a values grouped in order of priority, ended by rock type number. Each value in the string is separated with underscore.

Here, we briefly explain the procedure used in binning K_d values. The same method is used in binning K_a values. To simplify the Marfa input, the combination of the computed K_d values is discretized in "states". The states are created using the following procedure:

- First, **K_d** values are categorized based on Rock Type. Second, the minimum and maximum value of all the calculated K_d values of the same **rockType** is calculated over time-space domain.

- Then K_d values are divided in equally sized bins, based on the minimum and maximum values calculated above.

- All the K_d values calculated will be converted to bin values based on the **min/max** value calculated and the **number of bins** defined.

- Each unique combination of K_d/K_a bin values is considered a new "state". For example, let us consider a radionuclide characterized by a pair of K_d/K_a values. If these are divided in 5 bins, this will result in 25 states. All the states that are not seen by any pathline and particle position will be ignored though.

The states are written to the *kdbin.dat* file. The particle trajectory file is processed and for each segment in each trajectory a sequence of states is written to the *kdhistory.dat*. The N states seen by a segment/particle position are written to thee file. These states are accompanied by the "activation-time". Since the first time is always 0 it is left out, resulting in N-1 times per segment. The output can be written in different time units (timeUnit): years ("y") or seconds ("s").

timeStepInfo

The time stepping used in the iFM reference run is configured using the **timeStepInfo** dictionary. Note that the whole time range [*iniTime*, *endTime*] needs to have a chemistry applied. When the run time is changed, it is likely that the chemistry periods also need to be changed.

Analytical solution for radionuclide transport in a dual-porosity system with changes in background geochemistry

This appendix summarises the results of a collaborative work done by Dr. Daniel Fernàndez-Garcia, of the Universitat Politècnica de Catalunya, and Amphos 21. The work aims at getting insights into the influence that changing sorption properties have on the late-time behaviour of radionuclide break-through curves. The analytical solution developed here is intended to become a standard benchmark for any dynamic K_d application, and therefore a short summary of the work is included here. A more detailed account of the work will be provided in a scientific manuscript that is in preparation.

B1   Problem statement

Let us consider a single thin fracture embedded in a porous rock saturated with saline groundwater containing a large amount of Sodium (see Figure B-1). At this instant, a similar but more diluted groundwater enters continuously into the fracture with a contaminant pulse of radionuclides. We consider the radionuclides to be characterized by Cesium. This water enters through the inlet of the fracture and gradually penetrates into the matrix, triggering changes in the Cesium retention properties. As a result, the partitioning coefficient of Cesium changes with space and time. We intent to analyse analytically the late-time behaviour of the Cesium concentrations at the outlet of the fracture.
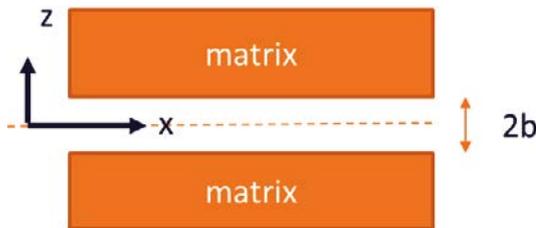

Figure B-1. *Schematic of the problem.*

B2   General transport equations

We consider that transport can be described by the advection-dispersion equation of reacting species. In a multi-porosity system formed by the fracture and the matrix, the transport of each chemical species can be described by two coupled transport equations, one for the fracture and one for the porous matrix. The coupling is provided by imposing equal concentrations of the chemical species at the interface between the fracture and the matrix. The transport of Cesium and Sodium along the fracture is

$$\frac{\partial C_f}{\partial t} + \frac{q_c}{b} = -v\frac{\partial C_f}{\partial x} + D_f\frac{\partial^2 C_f}{\partial x^2}$$

<div align="right">Equation B-1</div>

$$\frac{\partial N_f}{\partial t} + \frac{q_N}{b} = -v\frac{\partial N_f}{\partial x} + D_f\frac{\partial^2 N_f}{\partial x^2}$$

<div align="right">Equation B-2</div>

Where v is the groundwater velocity along the fracture, D_f is the diffusion coefficient, and C_f and N_f refer to concentration of Cesium and Sodium in the fracture, respectively. The terms q_c and q_N are the mass fluxes of Cesium and Sodium occurring at the interface between the fracture and the matrix, respectively. These fluxes are determined by Fick's law as

$$q_c = -\phi_m D_m \frac{\partial C_m}{\partial z}\bigg]_{z=b}$$

<div align="right">Equation B-3</div>

$$q_c = -\phi_m D_m \frac{\partial N_m}{\partial z}\bigg]_{z=b}$$

<div align="right">Equation B-4</div>

Where ϕ_m is the porosity of the porous matrix, and D_m is the diffusion coefficient associated with the matrix. Solute transport in the porous matrix is assumed to be governed by diffusion. Thus, the transport of Cesium and Sodium in the porous matrix is written as

$$\frac{\partial C_m}{\partial t} = D_m \frac{\partial^2 C_m}{\partial z^2} - r \qquad\qquad \text{Equation B-5}$$

$$\frac{\partial N_m}{\partial t} = D_m \frac{\partial^2 N_m}{\partial z^2} + r \qquad\qquad \text{Equation B-6}$$

Where r is the reaction rate due to the cation exchange process, and C_f and N_f refer to concentration of Cesium and Sodium in the porous matrix, respectively. In order to solve these system of transport equations, two additional equations are required. These equations are derived from the chemical reaction laws governing the ion-exchange process, whose chemical reaction is written as

$$C_m + XN_m = N_m + XC_m \qquad\qquad \text{Equation B-7}$$

Assuming that Cesium and Sodium are in local chemical equilibrium we have that

$$K = \frac{N_m \times XC_m}{C_m \times XN_m} \qquad\qquad \text{Equation B-8}$$

Where K is the selectivity coefficient or the equilibrium constant between the sorbed and solution phase. We have assumed that the selectivity coefficient is constant. The other equation is provided by the definition of the cation-exchange capacity, γ, which is assumed also to be a constant property,

$$\gamma = XN_m + XC_m \qquad\qquad \text{Equation B-9}$$

Given appropriate initial and boundary conditions, these system of nonlinear transport equations can be solved. Here, we assumed that initially the fracture and the matrix contain a large amount of Sodium in solution, denoted as N_0. Then, a more diluted groundwater is continuously released into the fracture at time $t = 0$. This new groundwater chemical system gradually penetrates into the matrix, triggering changes in the retention properties. In addition, a pulse of Cesium contamination enters the fracture at time $t = 0$ with duration T_0. These initial and boundary conditions are formally written as

Fracture system:

$$C_f(x = 0, t) = C_{inj}\, \Pi(t - T_0) \qquad N_f(x = 0, t) = N_{inj}$$

$$C_f(x = \infty, t) = 0 \qquad\qquad\qquad N_f(x = \infty, t) = N_0$$

$$C_f(x, t = 0) = 0 \qquad\qquad\qquad N_f(x, t = 0) = N_0 \qquad\qquad \text{Equation B-10}$$

Where Π is the box function defined as $\Pi(t{-}T_0) = H(t){-}H(t{-}T_0)$, being H the Heaviside function.

Porous matrix system:

$$C_m(x, z = b, t) = C_f(x, t) \qquad N_m(x, z = b, t) = N_f(x, t)$$

$$C_m(x, z = \infty, t) = 0 \qquad\qquad N_m(x, z = \infty, t) = N_0$$

$$C_m(x, z, t = 0) = 0 \qquad\qquad N_m(x, z, t = 0) = N_0 \qquad\qquad \text{Equation B-11}$$

B3   Conservative components

The general transport equations consist of 4 mass balance equations and 2 additional equations derived from chemical reaction laws. In this section, we decompose these system of equations into simpler problems. By defining u_m and u_f as the sum of Sodium and Cesium at any given time and position,

$$u_m = C_m + N_m \qquad\qquad \text{Equation B-12}$$

$$u_f = C_f + N_f \qquad\qquad \text{Equation B-13}$$

we see that these two chemical components follow a conservative transport equation (without reactions). That is to say that these components behave as a conservative species. These can be easily derived by summing Equation B-1 and Equation B-2 and Equation B-6 and Equation B-7, which yields,

Mass balance in the fracture:

$$\frac{\partial u_f}{\partial t} + \frac{q_u}{b} = -v\frac{\partial u_f}{\partial x} + D_f\frac{\partial^2 u_f}{\partial x^2} \qquad\qquad q_u = -\phi_m D_m \qquad\qquad \text{Equation B-14}$$

With initial and boundary conditions given by

$$u_f(x = 0, t) = N_{inj} + C_{inj}\Pi(t - T_0)$$

$$u_f(x = \infty, t) = N_0$$

$$u_f(x, t = 0) = N_0 \qquad\qquad \text{Equation B-15}$$

Mass balance in the porous matrix:

$$\frac{\partial u_m}{\partial t} = D_m\frac{\partial^2 u_m}{\partial z^2} \qquad\qquad \text{Equation B-16}$$

Subject to

$$u_m(x, z = b, t) = u_f(x, t)$$

$$u_m(x, z = \infty, t) = N_0$$

$$u_m(x, z, t = 0) = N_0 \qquad\qquad \text{Equation B-17}$$

This coupled system of transport of equations is the same system of equations as those proposed by Tang et al. (1981) for treating conservative transport along a fracture system. Hence, the solution of the conservative components can be derived in a similar fashion but subject to different initial and boundary conditions. Interestingly, an explicit expression can be found assuming that $D_f = 0$ and $u_f(x = 0, t) \approx N_{inj}$. In this case, we obtain the following solutions.

Solution for the matrix:

$$\frac{u_m(x, z, t) - N_0}{N_{inj} - N_0} = \text{erfc}\left(\frac{\omega(x, z)}{\sqrt{t - \frac{x}{v}}}\right), \qquad t > x/v \qquad\qquad \text{Equation B-18}$$

Solution for the fracture:

$$\frac{u_f(x, t) - N_0}{N_{inj} - N_0} = \text{erfc}\left(\frac{\omega(x, b)}{\sqrt{t - \frac{x}{v}}}\right), \qquad t > x/v \qquad\qquad \text{Equation B-19}$$

Where

$$\omega(x, z) = \left(\frac{x\phi_m\sqrt{D_m}}{2v\,b} + \frac{z - b}{2\sqrt{D_m}}\right) \qquad\qquad \text{Equation B-20}$$

B4   Partitioning coefficient

Let us first examine how the radionuclide partitioning coefficient evolves with time as a function of the conservative components. Defining the partitioning coefficient as

$$K_d = \frac{XC_m}{C_m} \qquad\qquad \text{Equation B-21}$$

Substituting Equation B-11, Equation B-9 and Equation B-8 into Equation B-21 we have

$$K_d = \frac{XC_m}{C_m} = \frac{\gamma\,K}{u_m - C_m + KC_m} \qquad\qquad \text{Equation B-22}$$

Considering that Cesium is in trace concentrations, the partitioning coefficient can be approximated as

$$K_d = \frac{XC_m}{C_m} \approx \frac{\gamma \ K}{u_m} \qquad \qquad \text{Equation B-23}$$

By introducing Equation B-18 into Equation B-23 we can examine the evolution of K_d with time.

Figure B-2 shows the evolution of K_d as a function of time at three different z coordinates. These curves have been computed using the parameters listed in Table B-1 and the conceptual model is the same used in a previous project to assess the implementation of the dynamic K_d approach in dual porosity media. We see that the K_d increases with time from a value of

$$K_d^0 = \frac{\gamma \ K}{N_{inj}} \qquad \qquad \text{Equation B-24}$$

Table B-1. Parameters of the single fracture-matrix system.

Symbol	Quantity	Value	Unit
b	Half of the fracture aperture	1.58×10^{-3}	m
L	Fracture length	0.5	m
Φ	Matrix porosity	1×10^{-2}	–
v	Groundwater velocity in fracture	24.1	m/y
α_L	Longitudinal dispersivity	2×10^{-4}	m
D_M	Molecular diffusion in free water	1×10^{-9}	m²/s
τ	Tortuosity in the rock matrix	1×10^{-1}	–
ρ_s	Bulk density of the rock matrix	$2\,600$	Kg/m³

At late times, we have that K_d is proportional to the square root of time $K_d \propto \sqrt{t}$. This is consistent with a series expansion of Equation B-24, which yields

$$K_d \approx \frac{\gamma \ K}{2(N_0 - N_{inj})\omega(x,z)} \sqrt{\pi \left(t - \frac{x}{v}\right)} - \frac{\gamma \ K \ N_{inj}}{4(N_0 - N_{inj})^2 \omega^2(x,z)} \pi \left(t - \frac{x}{v}\right) + \cdots \quad \text{Equation B-25}$$
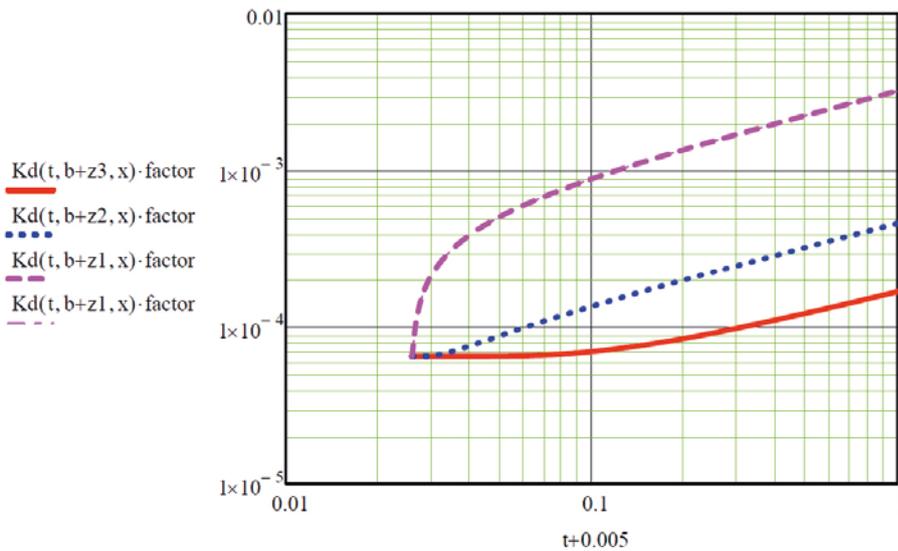

Figure B-2. *Evolution of K_d with time for $z = 0.0397$ m, 0.0139 m, 0.00198 m.*

B5 Matrix and fracture concentrations: A perturbation framework

The complicated part here is to get Cm and Cf from the conservative components. Unfortunately, there is not a simple expression to do this and one needs to solve a coupled system of partial differential equations. The gain from the previous system of equations is that by using conservative equations the number of partial differential equations is reduced. The mass balance of Cesium in the fracture system remains the same

$$\frac{\partial C_f}{\partial t} + \frac{q_c}{b} = -v\frac{\partial C_f}{\partial x} + D_f\frac{\partial^2 C_f}{\partial x^2} \qquad q_c = -\phi_m D_m \frac{\partial C_m}{\partial z}\bigg]_{z=b} \qquad \text{Equation B-26}$$

With initial and boundary conditions

$$C_f(x = 0, t) = C_{inj}$$

$$C_f(x, t = 0) = 0$$

$$C_f(x = \infty, t) = 0$$

But the mass balance in the porous matrix is simplified as it follows. Knowing that the chemical reaction is monovalent in this case with stoichiometric coefficient equal to unity, we have

$$r = \frac{\partial}{\partial t} X C_m = \frac{\partial}{\partial t} K_d C_m \qquad \text{Equation B-27}$$

Substituting Equation B-27 into Equation B-5 we have

$$\frac{\partial}{\partial t}(R C_m) = D_m \frac{\partial^2 C_m}{\partial z^2} \qquad R = 1 + K_d \qquad \text{Equation B-28}$$

subject to initial and boundary conditions

$$C_m(x, z = b, t) = C_f(x, t)$$

$$C_m(x, z = \infty, t) = 0$$

$$C_m(x, z, t = 0) = 0$$

The difficulty of these coupled system of equations resides in that the retardation factor depends on the conservative component solution, which changes in space and time. An analytical solution is not possible but these system of equations can be solved by using the perturbation method. The perturbation method estimates the deviation of the solution with respect to a known solution. In this case, we consider the solution obtained with a constant retardation factor given by $R^0 = 1 + K_d^0$ as the known solution. That is, the problem posed by the following mass balance equations

$$\frac{\partial C_f^0}{\partial t} + \frac{q_c^0}{b} = -v\frac{\partial C_f^0}{\partial x} + D_f\frac{\partial^2 C_f^0}{\partial x^2} \qquad q_c^0 = -\phi_m D_m \qquad \text{Equation B-29}$$

$$R^0 \frac{\partial C_m^0}{\partial t} = D_m \frac{\partial^2 C_m^0}{\partial z^2} \qquad \text{Equation B-30}$$

Considering that the concentrations of Cesium and the corresponding retardation factor can be expressed as the deviation from the known solution, we have

$$C_f = C_f^0 + C_f' \qquad \text{Equation B-31}$$

$$C_m = C_m^0 + C_m'$$

$$R = R^0 + R'$$

Substituting this into Equation B-29 and Equation B-30 and neglecting higher-order terms we have that the perturbation problem is the solution of the following coupled linear system of equations

$$\frac{\partial C_f'}{\partial t} + \frac{q_c'}{b} = -v\frac{\partial C_f'}{\partial x} + D_f\frac{\partial^2 C_f'}{\partial x^2} \qquad q_c' = -\phi_m D_m \qquad\qquad \text{Equation B-32}$$

$$R^0\frac{\partial C_m'}{\partial t} = D_m\frac{\partial^2 C_m'}{\partial z^2} - f(x,z,t) \qquad f(x,z,t) = \frac{\partial}{\partial t}\left(R' C_m^0\right) \qquad\qquad \text{Equation B-33}$$

At this stage, we note that the solution of perturbation problem depends on the solution of the porous matrix concentrations of Cesium with a constant retardation factor. In the following section we will solve this key problem. This solution is then used to get the late-time behaviour of concentrations.

B6 Matrix and fracture concentrations with constant retardation factor

It is convenient to define the following dimensionless variables:

Normalized time:

$$T = t\frac{v}{L}$$

Normalized z coordinate (along matrix):

$$Z = \frac{z}{B\sqrt{D}}$$

Normalized x coordinate (along fracture):

$$X = \frac{x}{L}$$

Peclet number:

$$P = \frac{L\,v}{D_f}$$

Damköhler number:

$$D = \frac{D_m L}{v\,R^0 B^2}$$

Matrix capacity:

$$\beta = \beta_0\sqrt{D}$$

$$\beta_0 = \frac{\phi_m R^0 B}{b}$$

Where B and L are characteristic length scales of the problem in the z and x coordinate. The Peclet number is the ratio of fracture diffusion time-scale to the advection time-scale. The Damköhler number is defined here as the ratio of advection time-scale to the matrix diffusion time-scale.

We will first solve the reference problem with a constant retardation factor given by the initial conditions and then we will solve the perturbation solution. In this context, Equation B-29 and Equation B-30 read as

$$\frac{\partial C_m^0}{\partial T} = \frac{\partial^2 C_m^0}{\partial Z^2} \qquad\qquad \text{Equation B-34}$$

$$\frac{\partial C_f^0}{\partial T} + \beta\left.\frac{\partial C_m^0}{\partial Z}\right]_{Z=a} = -\frac{\partial C_f^0}{\partial X} + \frac{1}{P}\frac{\partial^2 C_f^0}{\partial X^2} \qquad\qquad \text{Equation B-35}$$

Subject to

$$\frac{dC_m^0}{dZ} = 0 \quad at\ Z = 0$$

$$C_m^0 = C_f^0 \quad at\ Z = a$$

Note that the origin of the z coordinate is not set at the center of the fracture but at the bottom of the porous matrix. The solution of Equation B-34 is

$$\bar{C}_m^0(X, Z, s) = \bar{C}_f^0(X, s) \frac{\cosh(\sqrt{s}\,Z)}{\cosh(\sqrt{s}\,a)}$$

Equation B-36

Where the overbar denotes the Laplace transform, defined as

$$\bar{C}(s) = \int\limits_0^\infty C(t)e^{-st}dt$$

Equation B-37

The solution in the fracture system for a continuous injection is

$$\bar{C}_f^0(X, s) = C_{inj} \frac{1}{s} \exp\left(\frac{XP}{2} \left(1 - \sqrt{1 + \frac{4}{P}F(s)} \right) \right)$$

Equation B-38

Where

$$F(s) = s\left(1 + \beta\,\bar{g}_0(s)\right)$$

Equation B-39

The function $\bar{g}_0(s)$ is the Laplace transform of the memory function. This expression is general and can be used not only for a fracture system but also for any multirate mass transfer problem. The only thing is that one needs to use the proper memory function. For a finite matrix:

$$\bar{g}_0(s) = \frac{1}{\sqrt{s}}\tanh(\sqrt{s}\,a)$$

Equation B-40

This means that the mass flux exchange between the matrix and the fracture is characterized by a gradient that can be derived from Equation B-36 as

$$\left.\frac{\partial \bar{C}_m^0}{\partial Z}\right|_{Z=a} = s\,\bar{C}_f^0(X, s)\bar{g}_0(s)$$

Equation B-41

B7 Late-time behaviour

In this section we analyse the late-time behaviour of the concentrations of Cesium at the outlet of the fracture. An approximate solution valid at late times can be obtained in the Laplace space by taking $s \rightarrow 0$. That is to say that at large times the concentration of Cesium in the fracture is

$$C_f^0(X, T) = \mathcal{L}^{-1}\left\{\lim_{s\to 0}\bar{C}_f^0(X, s)\right\}$$

Equation B-42

Knowing that

$$\lim_{s\to 0}\bar{C}_f^0(X, s) = C_{inj}\frac{1}{s}(1 - X\beta s\bar{g}_0(s))$$

Equation B-43

We obtain

$$C_f^0(X, T) = C_{inj} - C_{inj}X\beta g_o(t)$$

Equation B-44

Introducing Equation B-43 into Equation B-42, we obtain that the large-time gradient of the concentrations of Cesium in the porous matrix at the interface for a continuous injection of Cesium in the fracture is

$$\lim_{t\to\infty}\left.\frac{\partial C_m^0}{\partial Z}\right|_{Z=a} = C_{inj}g_0(t)$$

Equation B-45

The solution for an instantaneous injection can be easily derived from the solution obtained with a continuous injection by the principle of superposition, which determines that the instantaneous solution is the derivative of the continuous injection solution. From this,

$$C_f^0(X, T) = -m_o X \beta \frac{dg_o(t)}{dt}$$

Equation B-46

$$\lim_{t \to \infty} \frac{\partial C_m^0}{\partial Z}\bigg]_{Z=a} = m_0 \frac{dg_0(t)}{dt}$$

Equation B-47

Where m_0 is the zeroth-order moment of the breakthrough curve. The inverse Laplace transform of the memory function g_0 is straightforward. For an infinite matrix, when a goes to infinity,

$$g_0(t) = \frac{1}{\sqrt{\pi t}}$$

Equation B-48

Introducing Equation B-38 into Equation B-46 we have that the Cesium concentration at late times follows a power law behaviour that scales with $C_f^0 \sim t^{-3/2}$,

$$C_f^0(X, T) = -\frac{m_o X \beta}{\sqrt{\pi}} t^{-3/2}$$

Equation B-49

We also need to solve the perturbation equation at late times. The perturbation solution in dimensionless variables can be written as

$$\frac{\partial C_m'}{\partial T} = \frac{\partial^2 C_m'}{\partial Z^2} - \frac{1}{R^0} \frac{\partial}{\partial T}(R' C_m^0)$$

Equation B-50

$$\frac{\partial C_f'}{\partial T} + \beta \frac{\partial C_m'}{\partial Z}\bigg]_{Z=a} = -\frac{\partial C_f'}{\partial X} + \frac{1}{P} \frac{\partial^2 C_f'}{\partial X^2}$$

Equation B-51

The diffusion equation (Equation B-50) has two parts. The first part is diffusion by Fick's law and the second part is an extra source term associated with the ion-exchange process. Let us consider that diffusion has already occurred and that the perturbative concentrations in the matrix are exclusively dictated by this extra source term caused by changes in the retention properties. In this case, integrating Equation B-50 we have

$$C_m' = -\frac{R'}{R^0} C_m^0$$

Equation B-52

At large times, when P is large and T is large enough, we have

$$\beta \frac{\partial C_m'}{\partial Z}\bigg]_{Z=a} = -\frac{\partial C_f'}{\partial X}$$

Equation B-53

Integrating,

$$C'_f(X = 1) = -\int_0^1 \beta \frac{\partial C_m'}{\partial Z}\bigg]_{Z=a} dX$$

Equation B-54

We note that Equation B-54 is equivalent to say that

$$C_f^0 = -\int_0^1 \beta \frac{\partial C_m^0}{\partial Z}\bigg]_{Z=a} dX$$

Equation B-55

The concentration of Cesium at the fracture is approximately equal to the sum of the zeroth-order solution and the first-order solution,

$$C_f = C_f^0 + C_f' = -\int_0^1 \beta \frac{\partial C_m^0}{\partial Z}\bigg]_{Z=a} dX - \int_0^1 \beta \frac{\partial C_m'}{\partial Z}\bigg]_{Z=a} dX$$

Equation B-56

Rearranging

$$C_f = C_f^0 + C_f' = -\beta \int_0^1 \frac{\partial C_m^0}{\partial Z} + \frac{R'}{R^0}\frac{\partial C_m^0}{\partial Z} + \frac{C_m^0}{R^0}\frac{\partial R'}{\partial Z}\bigg]_{Z=a} dX$$

Equation B-57

and

$$C_f = C_f^0 + C_f' = -\beta \int_0^1 \frac{R}{R^0}\frac{\partial C_m^0}{\partial Z} + \frac{C_m^0}{R^0}\frac{\partial R}{\partial Z}\bigg]_{Z=a} dX$$

Equation B-58

Where

$$R = 1 + \frac{\gamma \, K}{u_m}$$

Equation B-59

$$\frac{\partial R}{\partial Z}\bigg]_{Z=a} = -\gamma K \frac{1}{u_m^2}\frac{\partial u_m}{\partial Z}\bigg]_{Z=a}$$

Equation B-60

$$\lim_{t\to\infty} \frac{\partial C_m^0}{\partial Z}\bigg]_{Z=a} = m_0 \frac{dg_0(t)}{dt}$$

Equation B-61

$$C_m^0]_{Z=a} = C_f^0 = -m_o X\beta \frac{dg_o(t)}{dt}$$

Equation B-62

So that

$$C_f(X=1) = -m_0\beta \frac{dg(t)}{dt}\int_0^1 \frac{R}{R^0} - \frac{X\beta}{R^0}\frac{\partial R}{\partial Z}\bigg]_{Z=a} dX$$

Equation B-63

Knowing Equation B-61 this is also written as

$$C_f(X=1) = C_f^0(t)\int_0^1 \frac{R}{R^0} - \frac{X\beta}{R^0}\frac{\partial R}{\partial Z}\bigg]_{Z=a} dX$$

Equation B-64

This expression permits to analyse the late-time behaviour of the breakthrough curve of Cesium at the outlet of the fracture due to spatiotemporal changes in the retention capacity of the soil. This expression has two parts, the first part is the breakthrough curve obtained with a constant retardation factor; this concentration breakthrough curve scales with $C_f \sim t^{-3/2}$. The second term (the integral) is the deviation of the first curve due to the evolution of the retardation factor. Recalling that the retardation factor scales as $R \sim t^{1/2}$ and that these two components multiply each other, the resulting breakthrough curve scales as $C_f \sim t^{-3/2} t^{1/2} \sim t^{-1}$. These results are in agreement with the simulations carried out in a previous project focused on the implementation of the dynamic K_d approach.

SKB is responsible for managing spent nuclear fuel and radioactive waste produced by the Swedish nuclear power plants such that man and the environment are protected in the near and distant future.

skb.se